INVESTIGATION INTO THE DISPENSING - BASED FABRICATION PROCESS FOR TISSUE SCAFFOLDS

A Thesis Submitted to the College of

Graduate Studies and Research

in Partial Fulfillment of the Requirements

for the Degree of Master of Science

in the Department of Mechanical Engineering

University of Saskatchewan

Saskatoon

by

Hui David Ke

August 2006

PERMISSION TO USE

In presenting this thesis in partial fulfilment of the requirements for a Postgraduate degree from the University of Saskatchewan, I agree that the Libraries of this University may make it freely available for inspection. I further agree that permission for copying of this thesis in any manner, in whole or in part, for scholarly purposes may be granted by the professor or professors who supervised my thesis work or, in their absence, by the Head of the Department or the Dean of the College in which my thesis work was done. It is understood that any copying or publication or use of this thesis or parts thereof for financial gain shall not be allowed without my written permission. It is also understood that due recognition shall be given to me and to the University of Saskatchewan in any scholarly use which may be made of any material in my thesis.

Requests for permission to copy or to make other use of material in this thesis in whole or part should be addressed to:

Head of the Department of Mechanical Engineering

University of Saskatchewan

Saskatoon, Saskatchewan, S7N 5A9

ABSTRACT

Tissue engineering is a multidisciplinary subject aimed at producing the immunologically tolerant ‘artificial’ tissues/organs to repair or replace damaged ones. In this field, tissue scaffold plays a key role to support cell growth and new tissue regeneration. For fabrication of tissue scaffolds with individual external geometry and predefined inner structure, rapid prototyping (RP) systems based on fluid dispensing techniques have proved to be very promising. The present research conducted a comprehensive study on the dispensing-based fabrication process.

First of all, the scaffold materials are characterized in terms of their biocompatibility and flow behaviour. The biocompatibility of biomaterials of PLLA, PCL, collagen, chitosan, and gelatine is evaluated in terms of supporting neuron cells’ adhesion and outgrowth. Chitosan solution (2% w/v) in acetic acid is shown to be the most promising among the examined biomaterials for the fabrication of nerve tissue scaffolds. Its non-Newtonian flow behaviour is identified by using a commercial rheometer.

In the fabrication process, the flow rate of biomaterials dispensed, the profile of strand cross-sections, and the scaffold porosity are very important and must be precisely controlled. A model is developed to represent the flow rate of biomaterials dispensed under the assumptions that the flow is incompressible, steady, laminar, and axisymmetric. Also, the profile and size of line strands at different layers and portions are modeled based on the Young-Laplace equation. Thus the dispensing-based fabrication process can be predicted in terms of the flow rate and the scaffold porosity.

The effects of operation conditions on the fabrication result are identified theoretically and experimentally. Simulation result shows that a higher driving pressure, a higher temperature, and a larger needle diameter will result in a larger size of the strand cross-sections and lower scaffold porosity. The change pattern, however, is nonlinear, which is affected by the fluid surface tension and non-Newtonian flow behaviour of scaffold biomaterials.

To verify the effectiveness of the developed models, experiments were carried out on a commercial dispensing system (C-720, Asymtek, USA). To avoid the possible error derived from the temperature difference between the dispensing system and the rheometer, a new method is presented to characterize the fluid properties used for model predictions. Experimental results illustrate that the developed models, combined with the new identification method, are very promising to predict the dispensing-based fabrication process.

ACKNOWLEDGMENTS

I would like to express my sincere appreciation to those who have contributed to this research work, without whose work it would be impossible for this thesis. First, I would like to thank my supervisor, Prof. Dr. Daniel X.B. Chen. I am very grateful for everything he has done for me throughout my graduate program. His generous guidance, academic criticism, and continuous encouragement are incredible. I have learned a lot from him and hope that I can take it in my next stages of life successfully.

Then, I would like to extend the appreciation to those members of my Advisory Committee, Prof. Chris Zhang and Prof. Greg Schoenau. Their academic examinations and advice kept me on the right track.

Also, I would like to thank my wife, Xiaoli Yu, and my daughter, Jiaqi Ke, for their continuous love and patience. Their support on my spirit is beyond words.

Special thanks are given to Prof. Dr. David Schreyer and Mrs. R.L. Zhai from Cameco MS Neuroscience Research Center for their help on the biocompatibility experiments of scaffold biomaterials. Mr. Doug Bitner from the Dept. of Mechanical Engineering provided technical assistance on the dispensing experiments of scaffold fabrication. It was a pleasure and an honor to work with them.

It is acknowledged the financial support from Natural Science and Engineering Research Council (NSERC) of Canada and the Canada Foundation for Innovation (CFI) (through a research grant), and Dept. of Mechanical Engineering of the University of Saskatchewan (through the scholarship).

Finally, I would like to thank everyone who made my stay in Saskatoon the best it could be. I made a lot of great friends whose friendships will continue for many years.

TABLE OF CONTENTS

LIST OF TABLES

LIST OF FIGURES

Figure Page

Figure Page

NOMENCLATURE

A: cross-sectional area, m^2

D_n: diameter of dispenser needle, m

D_s: diameter of syringe, m

f : Darcy friction factor, dimensionless

g : gravitational acceleration, m/s^2

H_I (H_{II}): height of strand cross-section at Part I (Part II), m

$h(x)$: interface between fluid biomaterials and the ambient air, m

h' : the first derivative of $h(x)$ with respect to x

h'' : the second derivative of $h(x)$ with respect to x

K : consistency index, $Pa.s^n$

K_0 : curve-fitting parameter of consistency index, $Pa.s^n$

K_c : entrance loss correction factor, dimensionless

L_n: needle length, m

L_s: fluid height left in syringe, m

L_x: distance between two strands, m

$L_{strands}$: sum of strand length in the scaffold matrix, m

$M_{scaffold}$: mass of the tissue scaffold, kg

n : power law index, dimensionless

P_e : fluid pressure at the outlet of needle, Pa

P_g : air driving pressure, Pa

P_0 : ambient air pressure, Pa

P_s : fluid pressure at the outlet of syringe, Pa

Q: flow rate of fluid dispensed, m^3/s

R_1 , R_2: principal curvature radii of the air/fluid interface, m

r : radius in the needle, m

S_x (S_z): pore size in the X (Z) direction, m

T : temperature, ^oC

V_n : moving speed of the dispenser needle, m/s

$V_{scaffold}$: volume of the tissue scaffold, m^3

$V_{strands}$: volume of dispensed strands, m^3

$v_1(v_2)$: average velocity of flow at section 1 (section 2), m/s

W : width of the strand cross-section, m

W_I (W_{II}): width of strand cross-section at Part I (Part II), m

$\alpha_1(\alpha_2)$: kinetic energy correction factor at section 1 (section 2), dimensionless

$\dot{\gamma}$: shear rate, s^{-1}

λ : curve-fitting parameter of consistency index, ^oC

θ : fluid contact angle, degree

ρ : density of the fluid biomaterial, kg/m^3

σ : fluid surface tension, N/m

τ : shear stress, N/m^2

τ_{ij} : shear stress tensor, N/m^2

τ_w : shear stress at the needle wall, N/m^2

τ_y : yield stress, N/m^2

$\sum h$: sum of the pressure drops, m

Δp : pressure difference across the air/fluid interface, Pa

ΔP_n : pressure drop in the needle, Pa

CHAPTER 1 INTRODUCTION

1.1 Tissue Engineering

Tissue engineering is a multidisciplinary field which involves the 'application of the principles and methods of engineering and life sciences towards the fundamental understanding of structure-function relationships in normal and pathological mammalian tissues and the development of biological substitutes that restore, maintain or improve tissue function' [Shalak and Fox, 1988]. The content of tissue engineering spans a wide range of scientific and engineering fundamentals, involving biological sciences (e.g. cell biology, physiology, and wound healing), engineering disciplines (e.g. fluid dynamics, material science, mechanics, and chemical kinetics), clinical practices (e.g. surgery and transplantation, immunopathology, radiology), and various relevant biotechnologies (e.g. cell culture, cell separation, and gene transfer). One of the important goals of tissue engineering is to produce a supply of immunologically tolerant 'artificial' organ and tissue substitutes that can grow with patients. This will lead to a permanent solution to the damaged/diseased tissues and organs without the need of supplementary therapies, thus surpassing the limitations of conventional treatments based on organ transplantation and biomaterial implantation [Langer and Vacanti, 1993].

The process of developing an 'artificial' organ or tissue substitute is briefly presented in Figure 1.1 [Landers, 2002]. The desired implant area of a patient is scanned by computer tomography (CT) or magnetic resonance (MR); and the data obtained are imported into a CAD workstation in which a three dimensional (3-D) prototype is designed according to the specified biomedical requirements. The design information is then transferred to a rapid prototyping system to create a porous 3-D *tissue scaffold*. Once it is fabricated from biocompatible materials, biological agents (e.g. living cells, growth factors) are seeded onto the tissue scaffold. After a certain time period of cell culture and tissue regeneration outside the body (*in vitro*), the 'artificial' substitute is implanted into the human body and starts to resume its function within the body (*in vivo*). In this process, the tissue scaffold plays a key role in guiding the cell proliferation and tissue regeneration because natural cells and tissues lack the ability to grow in favored orientations [Langer and Vacanti, 1993].

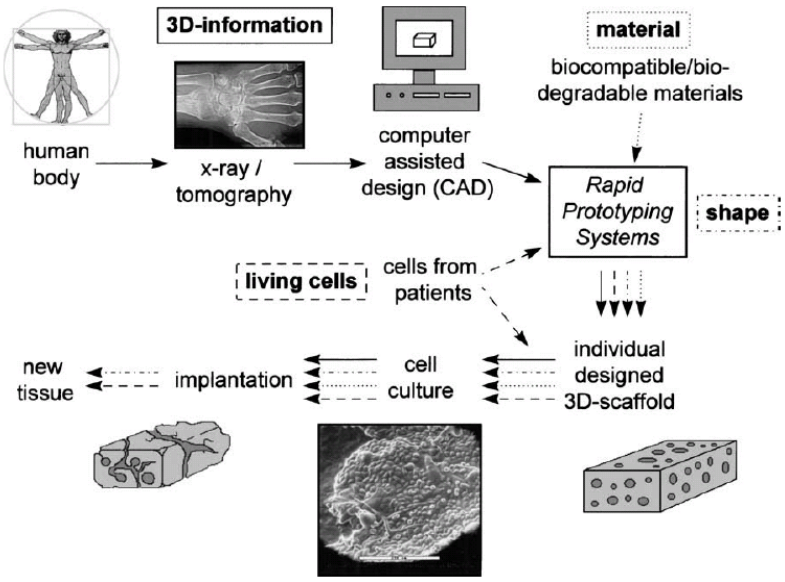

Figure 1.1 Development of an 'artificial' tissue substitute [Landers, 2002]

1.2 Tissue Scaffolds

Tissue scaffolds are used to provide support for cell attachment, proliferation, and differentiation, creating an extra-cellular matrix for tissue regeneration [Langer and Vacanti, 1993]. The support is either permanent or temporary in nature, depending on the application requirements. Temporary scaffolds are made from biodegradable materials, which can degrade slowly in the body (*in vivo*), leaving only the new regenerated tissues [Freed, 1994]. Permanent scaffolds remain in the body, working with ingrown tissues to form a polymeric/biological composite [Matsumoto, 2001].

Tissue scaffolds should possess proper macro- and micro-structural properties in order to favour not only cell adhesion and transportation but also tissue remodelling and regeneration [Mooney, 1992; Chen, 1997]. The following properties have been identified critical for tissue scaffolds [Freed, 1994; Grande, 1997; Hutmacher, 2001]:

Pore size and interconnectivity: A highly porous structure is necessary to allow cell proliferation, nutrient and waste transportation, and tissue integration. The micro-structure can be represented by using pore sizes and pore interconnectivity. Different types of tissues require scaffolds with different optimal micro-structures. For example, the pore size was suggested ranging from 200 to 400 μm for bone tissues [Robinson, 1995; Boyan, 1996], from 20 to 125 μm for skin tissues [Yannas, 1989]; and from 45 to 150 μm for liver tissues [Kim, 1998]. If the pore size is too small, cells will be unable to migrate within the scaffold. While the size is too large, cells can not bridge adjacent pores for proliferation, thus inhibiting effective new tissue regeneration.

Surface area and surface chemistry: To accommodate the large number of cells, the ratio of internal surface area to scaffold volume is desired to be large. Besides, the morphology and physiochemistry of the scaffold internal surface should also favour cell adhesion, migration, and reorganization [McClary, 2000].

Mechanical properties: As templates to guide tissue regeneration, scaffolds should have sufficient strength to maintain the space required for cell growth *in vitro* and to bear physiological loads imposed *in vivo*.

Degradation rate: Since most tissue scaffolds are used to provide only temporary support for cell growth, they will degrade *in vivo* once implanted. For this purpose, tissue scaffolds should be fabricated from biocompatible and biodegradable materials, such as agarose, chitosan, poly (lactic acid) (PLLA), and poly (ε-caprolactone) (PCL), etc. The degradation rate of a tissue scaffold should match the regeneration rate of new tissues in order to retain sufficient support.

Macro-structure: the macro-structure of tissue scaffolds should mimic the original shape and the physiological function of natural tissues.

1.3 Biomaterials and Fabrication of Tissue Scaffolds – A Critical Review

1.3.1 Biomaterials for Tissue Scaffolds

Biomaterials are of importance to tissue-engineered products. They are used to modify the cellular response (i.e., through specifically adhered molecules or the release of growth factors) or to support the cell growth and tissue regeneration (i.e., serve as tissue scaffolds). Some chemical and physical properties have been identified as critical for tissue engineering applications [Vert *et al.*, 1992; Freed *et al.*, 1994]:

Biodegradation and Bioresorption: Scaffold materials should fully degrade in order to leave only the new regenerated tissues, and residues need to be resorbed metabolically by the host tissues. A controlled degradation rate is critical to ensure that proper cell growth and tissue organization achieved before absorption.

Surface property: During the cell culture *in vitro* and implantation *in vivo*, the surface chemistry should favour proper cell attachment and growth onto tissue scaffolds. For this purpose, extracellular matrix proteins such as fibronectin and laminin could be added to basic scaffold biomaterials to modify the surface chemistry of tissue scaffolds.

Mechanical properties: A variety of tissue types require different scaffold materials with suitable mechanical properties, such as strength, viscoelasticity, brittleness, and ductility, etc. For example the bone tissue applications expect more rigid PCL scaffolds, while nerve tissue applications need soft chitosan scaffolds.

Considering these aforementioned properties, a large number of polymeric biomaterials, including synthetic and natural polymers, are being extensively investigated. The following is a brief introduction to the biomaterials that have been regulatory approved for tissue engineering applications [Hutmacher, 2000].

1.3.1.1 Synthetic Polymers

Poly (α-hydroxy esters) are the most commonly used synthetic polymers in tissue engineering, which include poly(lactic acid) (PLLA), poly(ε-caprolactone) (PCL), poly(glycolic acid) (PGA), and their copolymer poly(lactic-co-glycolic acid) (PLGA).

PGA is hydrophilic and sensitive to its environment, exhibits high crystallinity, and tends to degrade in aqueous solution; whereas PLLA is more hydrophobic, more soluble in organic solvents, and degrade more slowly than PGA [Middleton, 2000]. These two polymers can be copolymerized in different ratios to form a new polymer, PLGA, to optimize mechanical properties and degradation profile. Since PGA and PLA can not pack tightly, the PLGA copolymer has an amorphous structure and exhibits a faster degradation rate.

PCL is a semicrystalline biodegradable polymer. It has not been used quite often in tissue engineering due to its slower degradation kinetics. However, its mechanical properties and degradation profile can be modified by blending or copolymerizing with other polyesters [Middleton, 2000].

1.3.1.2 Natural Polymers

Two groups of natural polymers have been used in tissue engineering applications [Hayashi, 1994]: protein-based and carbohydrate-based polymers. Protein-based polymers include collagen and fibrin, and carbohydrate-based polymers include agarose, chitosan, hyaluronan, and alginate.

Collagen is the most abundant protein family in the body. Scaffolds made from collagen have been extensively used to load chondrocytes [Nehrer, 1997; Suh, 2000; Pieper, 2002] or mesenchymal stem cells (MSCs) [Wakitani, 1994] for cartilage tissue engineering.

Fibrin is a native hydrogel acting as a clinical fixative due to its natural role in wound healing. Fibrin has recently drawn scientific attentions serving as tissue scaffolds to deliver chondrocytes [Vanderploeg, 2004], mesenchymal stem cells (MSCs) [Bensaïd, 2003], or growth factors [Weiss, 2005] for repair of articular cartilage defects.

Gelatin is produced by partial hydrolysis of collagen extracted from skin, bones, cartilage, ligaments, etc. The biological origin of collagen-derived gelatin makes it an attractive choice for tissue engineering applications [Pesakova, 1990; Ponticiello, 2000].

Chitosan is derived from chitin, a natural polysaccharide found in crustaceans, fungi, and insects. It exhibits good biocompatibility and biodegradability [Onishi, 1999], and has been widely used in tissue engineering as well as the controlled drug delivery [Kim, 2003; Lee, 2004].

In summary, Table 1.1 listed a number of natural and synthetic polymers commonly used in scaffold fabrication, along with their clinical applications [Palsson and Bhatia, 2004].

Table 1.1 Natural and synthetic polymers for tissue engineering applications

Polymer	Materials	Clinical applications
Natural polymers	Protein-based polymers: collagen, fibrin	Cartilage, bone, skin, muscle, nerve, blood vessel, drug delivery, liver…
	Carbohydrate-based polymers: agarose, chitosan, hyaluronan, alginate	
Synthetic polymers	poly(lactic acid) (PLLA)	Cartilage, bone, valves, bladder, skin, muscle, nerve, blood vessel, cardiac tissue, drug delivery, liver…
	poly(ε-caprolactone) (PCL)	
	poly(glycolic acid) (PGA)	
	poly(lactic-co-glycolic acid) (PLGA)	
	Poly(2-hydroxyethyl methacrylate) (PHEMA)	Nerve, contact lenses, keratoprostheses orbital implants…

1.3.2 Fabrication Techniques for Tissue Scaffolds

How to fabricate tissue scaffolds with aforementioned properties? This question is drawing extensive attention from researchers worldwide. A number of fabrication techniques have been proposed and developed to date. These techniques can be generally classified into conventional fabrication and advanced Rapid Prototyping (RP).

1.3.2.1 Conventional Fabrication Techniques

Conventional fabrication techniques for tissue scaffolds include solvent casting, emulsion freeze-drying, melt moulding, and fiber bonding, etc.

Solvent casting creates a scaffold matrix from a suspension of PLLA solution with added salt particles. Once the suspension evaporated and the salt particles leached out, the desired porous 3-D structure is left behind [Mikos *et al.*, 1996]. This technology works only for thin scaffold membranes, otherwise it is very hard to remove the salt particles from inside the polymer matrix.

Emulsion freeze-drying builds a scaffold matrix from a water-in-oil emulsion of a solution of methylene chloride with PGA and added pure water. This emulsion was put into liquid nitrogen and then freeze-dried to produce the desired porous structure [Whang *et al.*, 1995]. This method is very sensitive to the processing parameters and equipment, and the pore size is unable to be controlled precisely.

Melt moulding uses mould fabrication technology to build a scaffold from PLGA powder and gelatin microspheres. The filled mould is heated above the glass-transition temperature of PLGA and moved away after cooling down, leaving behind only the desired tissue scaffold [Thompson *et al.*, 1995a]. Due to the destructive removal of moulds, this technique is unable to fabricate scaffolds in a consistent and reproductive way.

Some other techniques, such as fiber bonding, membrane lamination, and phase separation, are also falling into this category. Detailed description and review is provided by Widmer [1998].

The application of the conventional techniques is limited due to:

(1) Manual intervention: the fabrication process relies on operator's skill and experience, which is labour-intensive and time-consuming.

(2) Inconsistent manufacturing procedures, poor repeatability of the process performance.

(3) Use of toxic organic solvent: harmful residues may be left in thicker constructs.

(4) Shape limitations: only very thin (less than 300 μm) and simple scaffolds can be manufactured.

1.3.2.2 Advanced Rapid Prototyping (RP) Techniques

Rapid Prototyping (RP) techniques have been widely used in tissue scaffold fabrication, in which a 3-D tissue scaffold is fabricated by processing the solid sheet, liquid or powder materials layer by layer [Kruth, 1991; Chua, 1997]. In the following, the fluid dispensing-based RP systems for the scaffold fabrication are briefly reviewed and examined.

Three Dimensional Printing (3DP) [Bredt *et al.*, 1998]

3DP system incorporates inkjet printing technology to eject liquid binder onto a polymer powder surface. The binder dissolves and joins adjacent powder particles, and the jet head moves according to the CAD cross-sectional profile, forming the required layer. The process is repeated on successive layers to construct a 3-D structure. By means of the 3DP method, Kim *et al.* [1998] created porous scaffolds from poly-lactide-co-glycolide (PLGA) powder mixed with salt particles. These tissue scaffolds are cylindrical in shape (Diameter × Height = 8 mm × 7 mm) with pore size of 45–150 μm and a porosity of 60%. Zeltinger *et al.* [2001] also employed this

method to create poly (L-lactic acid) (PLLA) disc-shaped scaffolds measuring 10 mm in diameter and 2 mm in height. The scaffolds were constructed with two different porosities (i.e., 75% and 90%) and four ranges of the pore size (i.e., < 38, 38 – 63, 63 – 106, and 106 – 150 μm) to investigate the influence of pore size and porosity on cell adhesion and proliferation.

Fused Deposition Modeling (FDM) [Scott, 1991]

FDM system fabricates a scaffold from a fused fibre of thermoplastic material, which is deposited through a heated needle. The pore size of tissue scaffolds must be very small in order that the fibre strand can bridge across pores without additional support. By using the FDM method, Zein *et al.* [2002] produced poly-caprolactone (PCL) scaffolds with honeycomb-like structures and fully interconnected pores. The scaffolds were constructed with pore sizes ranging from 160 to 700 μm and porosities from 48% to 77%. To investigate the cell cultural response *in vitro,* Hutmacher *et al.* [2001] developed PCL scaffolds in rectangular layout (width × length × height = 25.5mm × 32mm × 13.5mm). In each layer, two different interlacing patterns (0º/60º/120º and 0º/72º/144º/36º/108º, respectively) were designed, while the scaffold porosity is maintained at a constant of 61%.

Three Dimensional Plotting (3D Plotting) [Landers *et al*, 2000]

3D plotting system builds 3-D scaffolds from a paste-like plotting medium. The dispenser head can be heated to a required temperature to improve the fluid flow behaviour. Landers and Mulhaupt [2000] fabricated agar hydrogel scaffolds with the 3D plotting method. Specifically, the agar solution was heated to 70 ^{o}C and dispensed in an aqueous gelatine solution with a temperature of 20^{o}C to form desired patterns. Density and polarity of the gelatine solution were

adjusted to compensate the influence of gravity on dispensed strands. Ang *et al.* [2002] developed a RP robotic dispensing system that works on the same principle as the 3D plotting, by which solutions of chitosan and chitosan-HA were extruded into a sodium hydroxide and ethanol medium to form desired 3-D scaffolds. In their study, it was found that the concentration of sodium hydroxide can significantly affect the adhesion between two dispensed layers.

Phase-change Jet Printing [Philbrook *et al*., 1996]

This system comprises two inkjet print heads which deliver different materials: one is for building the model matrix and the other one provides support for any unconnected or overhanging features. Melted microdroplets are generated from the heated jet heads, and deposited in a drop-on-demand manner. The microdroplets solidify on impact to form a bead. Overlapping of adjacent beads forms a line and overlapping of adjacent lines forms a cross-sectional layer. This process is repeated layer by layer until the 3-D matrix constructed. After that, the matrix is immersed in a selective solvent to wash away supporting materials, left over the physical scaffold in its desired shape.

Table 1.2 summarizes the fabrication methods described above, including both conventional ones and advanced RP ones, as well as their pros and cons. Compared to conventional fabrication techniques, the advanced RP techniques are drawing more attentions because of their flexibility and capability on precise control, customer design, and processing cost & time efficiency.

Table 1.2 Comparison of different fabrication methods for tissue scaffolds

Fabrication Technology	Pore size (μm)	Porosity (%)	Advantages	Disadvantages
Solvent casting and particle leaching	30-300	20-50	Large range of pore sizes, independent control of porosity and pore size.	Limited thickness, lack of mechanical strength, harmful organic solvent and porogens residue.
Freeze Drying	<200	<97	Highly porous structures, High interconnectivity.	Limited to small and uncontrolled pore sizes
Melt moulding	50-500	<80	Independent control of porosity and pore size, Macro shape control	High processing temperature needed, non-repeatable
Three - Dimensional Printing (3DP)	40-150	<90	High surface area to volume ratio, Independent control of porosity and pore size, Wide range of material selection	Limited to small pore sizes, lack of mechanical strength, harmful organic solvents
Fused Deposition Modeling (FDM)	150-700	<80	High surface area to volume ratio, Good compressive strengths, Solvent free	High temperature needed, require support for irregular shapes
Three - Dimensional Plotting (3-D Plotting)	200-500	40-65	Complete pore interconnectivity, Incorporation of biological agents into fabrication	Slow processing, Fluid viscosity dependent, plotting medium fluctuated
Phase-change Jet Printing	200-400	<90	Use dual dispensing head, flexible, support-free for irregular shapes	High temperature needed, time consuming, low accuracy, rough surface

1.3.3 Modelling of the Dispensing-based Fabrication Process

In the aforementioned RP fabrication process, there is a critical procedure, i.e., the dispensing of fluid biomaterials. Figure 1.2 illustrates schematically a typical dispensing process used in RP fabrication systems. The fluid biomaterial is delivered out of the needle in a controlled manner by pressurized air. Once dropped onto the substrate, the fluid biomaterial begins to spread and then coagulate into line strands. The strands can be laid down in different patterns at each layer, laminated vertically to form an interlacing 3-D scaffold.

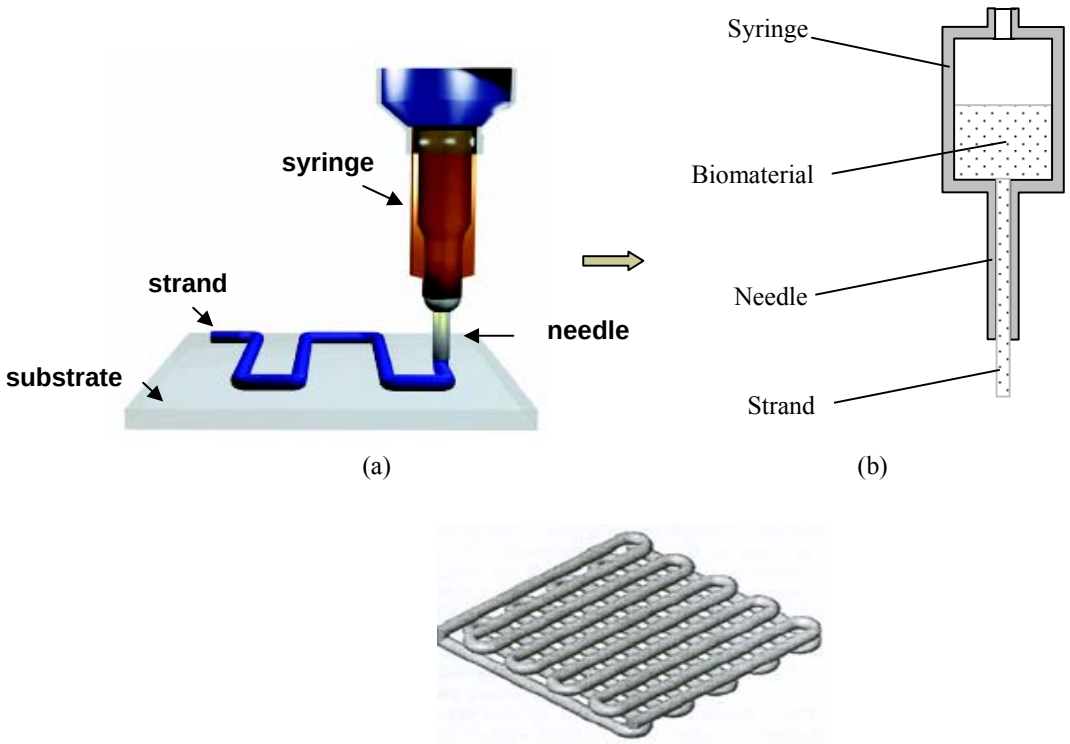

(a) (b)

(c)

Figure 1.2 A typical dispensing process in RP fabrication systems;
(a) Overview of the process, (b) internal structure of dispenser, (c) a 3-D scaffold

The dispensing-based RP techniques are very promising for tissue scaffold fabrication. The control of such a process, however, has proven to be a challenge task. Experimental result shows that in a fabrication process, the flow rate of biomaterial dispensed, thus the pore size and porosity of the scaffold developed, can be affected by many factors such as temperature, the air pressure applied to the dispenser, and the flow behaviour of the biomaterial. Unfortunately, the models, upon which the effects of aforementioned factors can be specified, are lack in literature. In existing studies, the desired scaffold microstructures (e.g. pore size, porosity) have to be ensured by trial and error. The ever-increasing demand for high quality tissue scaffolds has been spurring researchers to gain more insight into the dispensing-based fabrication process. Therefore, the development of such a model that can represent the fabrication process is essentially required, yet very difficult if taking into account the complex flow behaviour of scaffold biomaterials. Very few studies were carried out or reported on this specific research topic.

Vozzi *et al.* [2002] developed a model to predict the fabrication process under the assumption that the scaffold biomaterial is Newtonian fluid, and ignoring some other forces except air driving pressure. This model could be used to determine strand width and height, but it requires a priori knowledge of the cross-sectional profile. In a real fabrication process, however, the strand profile is affected by the biomaterial properties and the ambient temperature, thus it is unable to be assumed beforehand. Besides, in this model the dispensed biomaterial was assumed as Newtonian fluid. As reviewed earlier, scaffold biomaterials are usually high polymeric solutions. In dispensing process, they exhibit non-Newtonian flow behaviour, which is far different from the Newtonian fluids. Another major limitation of this model is that it is not valid

at low driving pressure, where the forces derived from surface tension, dynamic friction, and weight of biomaterials may significantly affect the fabrication process.

Too *et al.* [2002] developed a model to represent the scaffold porosity and the cross-sectional size of strands. In the model development, the cross-section of scaffold strands is assumed to be elliptical. Obviously, it is just an approximation. In addition, this model needs the weight of fabricated scaffolds, which is not available unless the fabrication process completed. Therefore, this model can not be used to PREDICT the fabrication process.

Finke *et al.* [2002] studied the effects of non-Newtonian flow behaviour of scaffold biomaterials on the dispensing process. The results showed that the temperature variation greatly changed the material flow behaviour, thus affecting the dispensing process. An attempt was made to model the extrusion force as a function of fluid viscosity and needle geometry, so as that the required driving pressure could be determined. This model, however, is limited by the assumption of constant fluid viscosity and ignoring the flow friction. As a result, it is not valid for non-Newtonian fluids because their viscosity depends not only on the temperature and pressure but also the shear rate and even the previous shear history.

Woodfield *et al.* [2004] proposed two models to predict the scaffold pore size and porosity. One is developed based on the assumption of circular cross-section of strand profiles, and the other one also needs to know the weight of tissue scaffolds. As concluded above, both of them are limited for tissue engineering applications.

In the context of electronics packaging, the flow behaviour of non-Newtonian fluids and its influence on the dispensing process have been investigated [Chen *et al*, 2000; 2004]. Some of the outcomes can be adapted and used in the present research. Meanwhile, it should be noted that scaffold materials are different from the fluids used in the electronics industry. Their flow behaviour needs to be characterized experimentally. And also, the dispensers used in tissue scaffold fabrication are always designed to be very small. A typical needle diameter of the dispenser head is in the range of 100 - 500 μm. As a result, the fluid surface tension will be involved in the dispensing process and affect the fabrication performance. In addition, it is known that the RP fabricated scaffolds are laminated by several strand layers, compared to only one layer in electronics packaging applications. How to determine the strand profile on upper subsequent layers is another issue that has to be addressed.

The review on the related literature shows that much effort has been put in the study of tissue engineering scaffolds. Also, it is seen that the characterization of scaffold biomaterials and the development of models to represent the dispensing-based fabrication process are two key issues, which will be addressed in this research.

1.4 Research Objectives

The present research is to investigate the dispensing-based fabrication process, with an emphasis on identifying the influence of various factors on the process performance. Specifically, the objectives to be achieved are proposed as follows:

(1) Characterizing scaffold biomaterials in terms of biocompatibility and flow behaviour.

A number of biomaterials have been investigated individually in literature for various tissue engineering applications. But for a given type of tissue, e.g. nerve, cartilage, or skin, there is a lack of study to evaluate and compare the material biocompatibility, namely, the suitability to perform with a host response in a specific application [Anderson, 1998]. This research will carry out a quantitative analysis on the biocompatibility of some biomaterials that are commonly used in nerve tissue engineering. The materials that best support cell adhesion, survival and proliferation will be selected for the scaffold fabrication.

The biomaterial solutions for scaffold fabrication usually exhibit non-Newtonian flow behaviour, in which the fluid viscosity is not a constant at a given temperature but depends on the shear rate in flow [Wilkinson, 1960; Barns, 1989; Chhabra and Richardson, 1999]. In this research, the flow behaviour of the scaffold biomaterial and its effect on the fabrication process will be investigated.

(2) Developing models to represent the dispensing-based fabrication process.

In the fabrication process of tissue scaffolds, the flow rate of the biomaterials dispensed, the profile of the strand coagulated, and the scaffold porosity are the most important indexes. These indexes can be influenced by several parameters, including the flow behaviour of the biomaterial solution, the operating conditions (e.g. temperature, air driving pressure), and the structure of dispenser head. In this research, models will be developed to represent the aforementioned indexes for the dispensing-based fabrication process, i.e., the flow rate, the strand profile, and the scaffold porosity.

(3) Identifying the effect of different parameters on the fabrication process.

Based on the models developed above, the effect of different parameters on the fabrication process will be investigated theoretically and experimentally. Particularly, a new method will be developed to characterize the biomaterial flow behaviour from the fabrication process, rather than from a rheometer. This method is to avoid the possible involvement of the error due to the temperature difference between the fabrication system and the rheometer used for the flow behaviour characterization.

1.5 Organization of Thesis

In total, there are seven chapters in this thesis. Besides this chapter, the rest is organized as follows:

Chapter 2 deals with a comparative study on the biocompatibility of scaffold materials, as applied to the nerve tissue engineering. The cell culture experiments are conducted by using thin films made from several biomaterials examined, respectively. Based on the experimental results, the biocompatibility is evaluated in terms of both cell adhesion and neurite outgrowth of DRG neurons on individual biomaterials.

In Chapter 3, the flow behaviour of a kind of scaffold biomaterial, i.e., Chitosan solution (2% w/v) in acetic acid, is measured and characterized. This material is very promising for nerve tissue repair applications, as shown in Chapter 2. Experiments were carried out on rheometer to identify the non-Newtonian flow behaviour of this material. Fluid parameters associated with the non-Newtonian flow behaviour, including the yield stress, viscous consistency index, and power law index, are characterized to serve the following model development.

Chapter 4 presents the development of a model to represent the flow rate of dispensed biomaterials in the scaffold fabrication process. In the model development, the fluid surface tension is taken into account to determine the fluid pressure at the outlet of the dispenser needle; the pressure drop and the velocity distribution in the needle are derived based on the knowledge of fluid mechanics. For model verification, experiments were conducted on a commercial

dispensing system (C-720, Asymtek, USA). Experimental results are presented in the chapter, along with the discussion.

In **Chapter 5,** models are developed to represent the profile of strand cross-sections and the scaffold porosity in the fabrication process. Based on these models, the profile and size of strand cross-sections at different layers and portions are determined numerically. Then the scaffold porosity is evaluated from the volume of dispensed strands and the one of whole scaffold. Simulations are carried out to discuss the effect of air driving pressure, temperature, and the dispenser needle diameter on the strand profile and scaffold porosity.

Based on the models developed in previous chapters, **Chapter 6** investigates the influence of different parameters on the performance of dispensing-based fabrication process. A new method is presented to characterize the scaffold biomaterial properties, in which the fluid properties are identified directly from a few dispensing experiments, instead of from a rheometer. Thus identified parameters were used to predict the dispensing-based fabrication process. The comparison between the predictions and the experimental results illustrates that those developed models, combined with fluid properties thus identified, are very promising for the prediction of fluid dispensing results.

Chapter 7 summarizes the conclusions from the present research. Suggestions and recommendations for possible future work are also presented in this chapter.

CHAPTER 2

COMPARATIVE STUDY ON MATERIAL BIOCOMPATIBILITY FOR NEURAL TISSUE ENGINEERING

The design and fabrication of tissue scaffolds begins with the proper selection of biomaterials. In tissue engineering, the requirements imposed on biomaterials vary with the tissue types considered. In this chapter, as applied to the repair of injured PNS tissue, the biocompatibilities of five scaffold materials, i.e., polylactic acid (PLLA), polycaprolactone (PCL), collagen, chitosan, and gelatin, are investigated and compared in terms of cell adhesion, proliferation, and neurite outgrowth. The objective is to identify the most promising biomaterial for use in the following research.

2.1 Introduction

Neural tissue engineering involves the nerve repair and regeneration for injured nerve system. Nerve injury may occur in either the central nervous system (CNS) or the peripheral nervous system (PNS). For CNS, the regeneration is essentially difficult due to physical (i.e., glial scar) and chemical (i.e., myelin proteins) inhibitors; but in PNS, the regeneration or repair is possible for small injury gaps [Schwab, 1998; Fry, 2001; Schmidt, 2003]. If the nerve injury is too large (e.g. gap > 10 mm), a common treatment recently used is that an autograft of nerve

tissue, taken from other parts of the patient body, is implanted to surgically bridge the gap between the proximal and distal nerve stumps. An alternative strategy is using an artificial neural scaffold to create a permissive conduit and favourable micro-environment for nerve regeneration [Heath, 1998; Schmidt, 2003]. Several requirements or properties have been identified as crucial for the biomaterials used for neural scaffolds [Gerburg *et al.*, 2003]: (1) allowing diffusion transport of nutrients and other molecules while preventing external cells from entering the conduit; (2) revascularizing fast enough in neural scaffolds to overcome nutrient transport limitations; (3) biodegrading slowly to maintain a stable support for the entire regeneration process; (4) be immunologically compatible with the host tissue; and (5) supporting cell adhesion and proliferation on neural scaffolds.

A number of biomaterials, including polycaprolactone (PCL), chitosan, and collagen, have been investigated individually in literature for nerve repair and regeneration, showing varying degrees of success [Flynn, 2003, Yu, 2004, Sundback, 2005]. However, there is a lack of study on comparing the biocompatibility of these materials. This chapter is to present such a study by looking into the biocompatibility of different materials in terms of supporting adhesion and proliferation of Dorsal Root Ganglia (DRG) neurons. In particular, thin films are created from individual applicant material and serve as a support for the growth of DRG neurons; and then the biocompatibility is evaluated by examining the adhesion, viability, and proliferation of the DRG neurons seeded onto different films.

2.2 Materials and Preparation

The scaffold materials examined in this study include PLLA, PCL, collagen, chitosan, and gelatin. All materials were purchased from Sigma-Aldrich Canada Ltd. (Toronto, ON. Canada) and used as received. The preparation of each material is listed as follows:

1) PLLA: dissolved in chloroform to form 5% (w/v) solution.
2) PCL: dissolved in chloroform to form 20% (w/v) solution.
3) Collagen: dissolved in 0.5 mol/L acetic acid to form 1% (w/v) solution.
4) Chitosan: dissolved in 0.2 mol/L acetic acid to form 2% (w/v) solution.
5) Gelatin: dissolved in sterile, distilled water (70°C) to form 10% (w/v) solution and then adjust the solution to pH = 7 by using sodium hydroxide solution, HEPES as buffer.

Each of the above solutions, with a volume of 250 μL, was applied to coat on the surface of a glass coverslip (22 mm × 22 mm) to form a thin film. These coverslips were maintained in glass dishes at room temperature until air dry, and then stored in a cold room at 4 ^{o}C.

2.3 Experiments

To monitor the outgrowth of nerve fibres *in vitro*, sensory neurons were isolated from the DRG of adult rats, along with the non-neuronal Schwann cells, which are known to support the growth of axons. Enriched primary Schwann cell cultures were prepared from adult rat sciatic nerve by enzymatic dissociation [Brockes, 1979]. Contaminated Schwann cells were removed

from cultures by density gradient centrifugation. Primary DRG neuron cultures were prepared by using collagenase and trypsin [Lindsay, 1988]. The cultures of both Schwann cells and DRG neurons were maintained in polystyrene dishes coated with poly-L-lysine in DMEM plus 10% horse serum. These dishes were kept in a humidified incubator at 37^{o}C, with an atmosphere of 5% carbon dioxide and 95% air.

After an initial culture period (2 weeks for Schwann cells, 5 days for DRG neurons), cells were transferred onto previously prepared coverslips, which were coated a thin film of individual materials. Both cell types were detached from flasks using trypsin/EDTA, counted, and seeded at a density of 5,000-50,000 cells/coverslip using a small volume of culture medium (75μL per coverslip). After allowing one hour for cell attachment, additional 1 mL of cell culture medium was added to each dish to submerge the entire coverslip. After one week in culture, the coverslips were rinsed three times in serum-free medium and fixed for histological processing in methanol at -20 ^{o}C (alternatively, in 1% paraformaldehyde in 0.1 M phosphate buffer). Cell-seeded coverslips were removed from the culture dishes, embedded in 10% polyvinyl alcohol, and mounted on gelatin-coated glass slides for immunocytochemical processing. Cells were fixed and stained with an antibody against the neuronal protein GAP-43 [Schreyer, 1991].

Cells were visualized with a Zeiss Axioskop microscope equipped with optical and fluorescence detection light. Total cell number was counted by labelling the nuclei with 20 μg/mL DAPI fluorescent dye (Molecular Probes) and extrapolating from cell densities measured in individual sections. Cell images were captured using a digital camera and analyzed by using Northern Eclipse workstation (Empix Imaging, ON. Canada).

2.4 Results and Discussion

The adhesion and growth of DRG neurons on coated coverslips was observed through the Zeiss Axioskop microscope. The cell images were captured by mounted digital camera and showed typically in Figure 2.1 (a-e) for individual scaffold materials. The large black dots are image of DRG cells left on scaffold films. Those cells that did not adhere onto thin films have been washed away in the previous rinse process. The tree-like branches around those black dots are image of the outgrown neurites. The longer branches imply the better the neurites grow and extend. It can be seen that black dots and branches appeared on every pictures, indicating that DRG cells can adhere and extend neurites on all these scaffold materials.

By using the Northern Eclipse workstation, the DRG cell number attached and neurite length outgrown on thin films are measured individually. Both of them are important indexes to evaluate material biocompatibility [Flynn, 2003; Yu, 2004; Sundback, 2005]. The results obtained are shown in Figure 2.2(a) for the average cell number (cells/cm^2) and Figure 2.2(b) for the average neurite length (μm/cell).

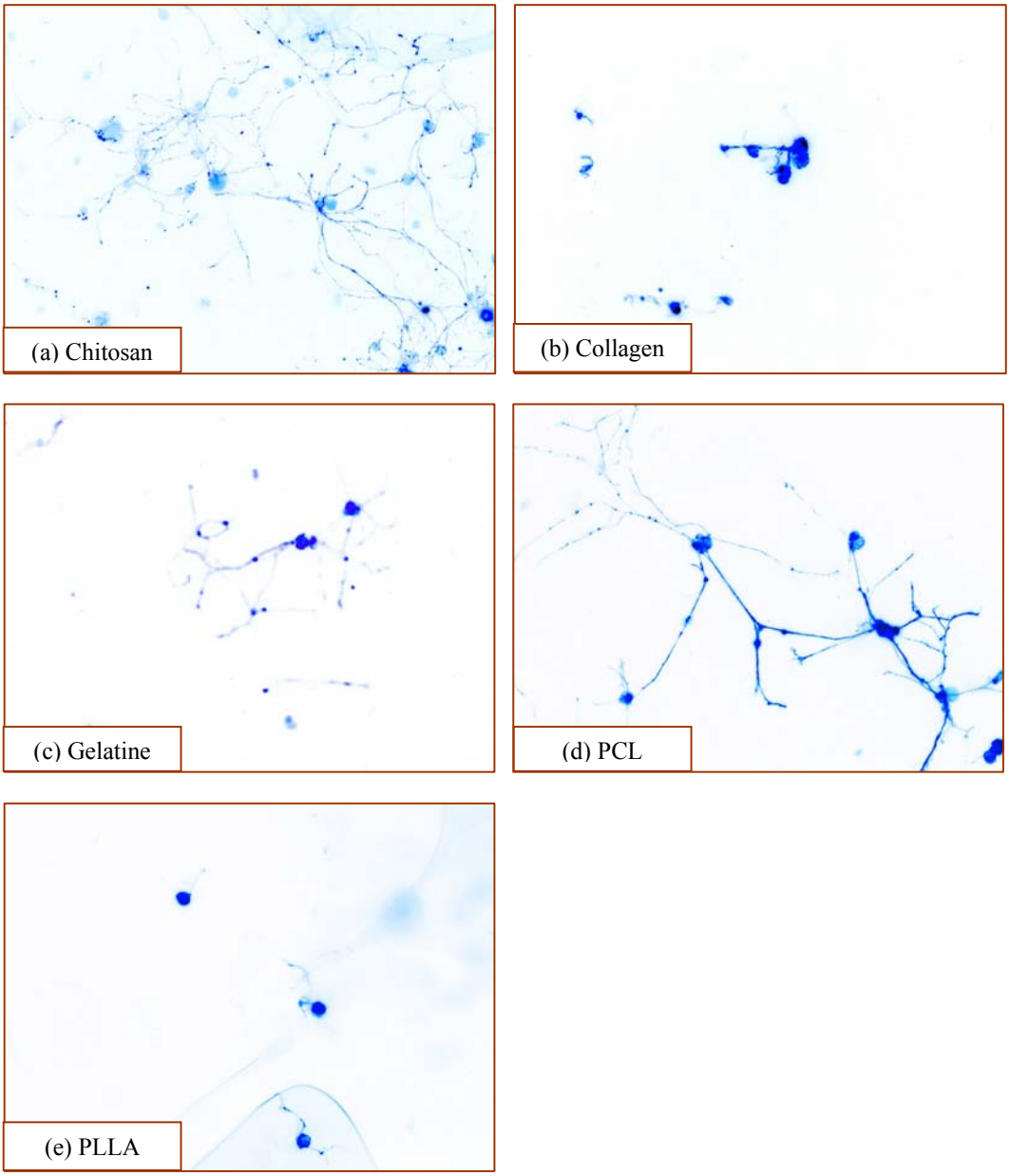

Figure 2.1 Comparison of cell response on different scaffold materials. Fluorescent microscopy images show that DRG cells adhered and neurites extended on all thin films, but with different extents.

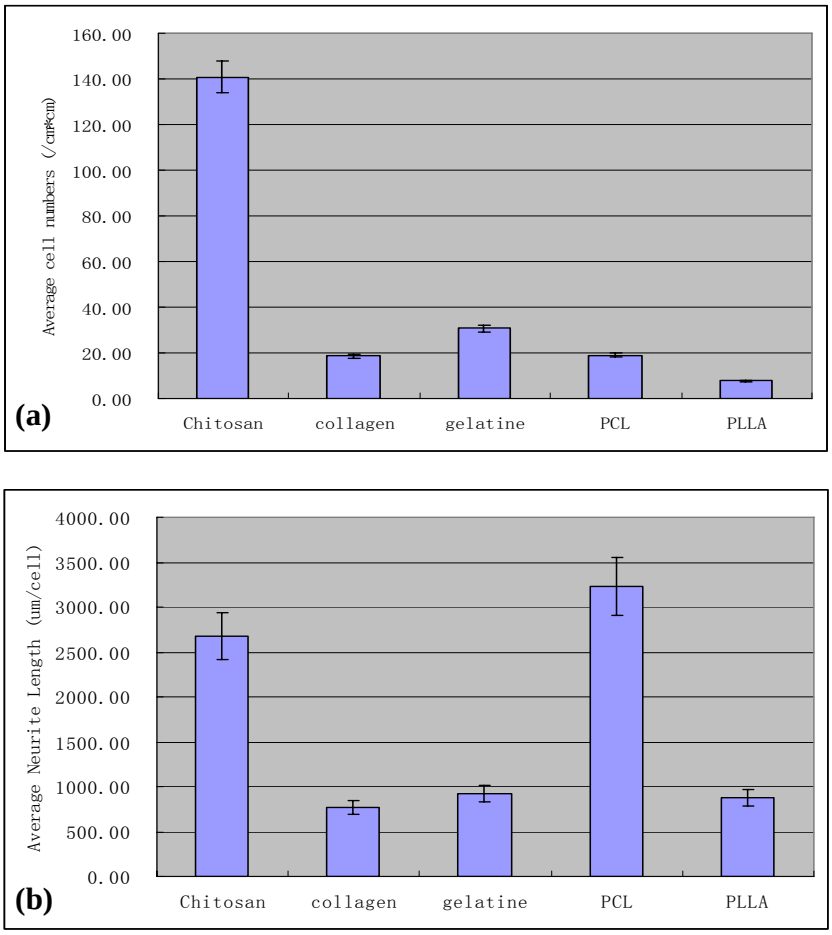

Figure 2.2 DRG cell adhesion and neurite outgrowth after one week of culture on films of different materials: (a) Average cell number (cells/cm^2), (b) Average neurite length (μm/cell).

Figure 2.2(a) shows that all materials can support cell adhesion, but cells adhered to the chitosan film (around 140 cells/cm^2) are much more than what adhered to any other material (less than 40 cells/cm^2). There is no much statistical difference among those rest materials. On the film surface of PLLA, the majority of cells were washed away during the rinse process (less than 10 cells/cm^2 left), reflecting poor cell adhesion. DRG neurite outgrowth is assessed by measuring the average neurite length on each cell. As shown in Figure 2.2(b), PCL and chitosan

films have significantly longer neurite extension than the films of collagen, gelatin, and PLLA. There is no statistical difference found among the collagen, gelatine, and PLLA films in terms of neurite length.

Taking into account both cell adhesion and neurite outgrowth, it can be concluded that chitosan, which held the largest average number of cells adhered and the second longest average length of neurite outgrown, seems to be more suitable for supporting nerve regeneration *in vitro* than other materials. In contrast, both cell numbers and neurite length in the materials of collagen, gelatin, and PLLA are generally low, suggesting their poor support for nerve repair and regeneration.

2.5 Summary

This chapter presented a comparative study on the biocompatibility of materials of PLLA, PCL, collagen, chitosan, and gelatin, in the application of PNS nerve repair and regeneration. Quantitative analysis was carried out to evaluate both cell adhesion and neurite outgrowth of dissociated adult DRG neurons. The results showed that chitosan seems to be the best candidate among the scaffold materials examined in this study. It shall be very promising in the applications of PNS nerve repair and regeneration.

CHAPTER 3

CHARACTERIZATION OF FLOW BEHAVIOUR OF SCAFFOLD BIOMATERIAL

Biomaterials used in scaffold fabrication are usually high polymeric solutions and exhibit non-Newtonian flow behaviour. The characterization of such flow behaviour is essential as it may significantly affect the fabrication process. In this chapter, the flow behaviour of chitosan solution (2% w/v dissolved in acetic acid) is investigated and characterized by using a rheometer. It is noted that this material is one of the most promising biomaterials used in PNS nerve repair and regeneration as examined in Chapter 2.

3.1 Introduction to non-Newtonian Flow Behaviour

If a fluid exhibits non-Newtonian flow behaviour, the relationship between the shear stress and shear rate is not linear at a give temperature, but depends on the shear rate and even on the previous shear history the fluid experienced. According to the nature of flow behaviour, non-Newtonian fluids can be classified into three types: (1) purely viscous time-independent, (2) purely viscous time-dependent, and (3) viscoelastic [Skelland, 1967; Barns, 1989; Chhabra and Richardson, 1999].

In purely viscous time-independent fluids, the shear stress and fluid viscosity are not affected by the previous shear history, but related to the shear rate in the flow. Figure 3.1(a) shows some non-linear flow curves of time-independent fluids, in which τ_y is the yield stress. According to the shear stress *vs.* shear rate relationship, these fluids can be further divided into Herschel-Bulkley fluid, Bingham plastic fluid, Pseudoplastic fluid, and Dilatant fluid.

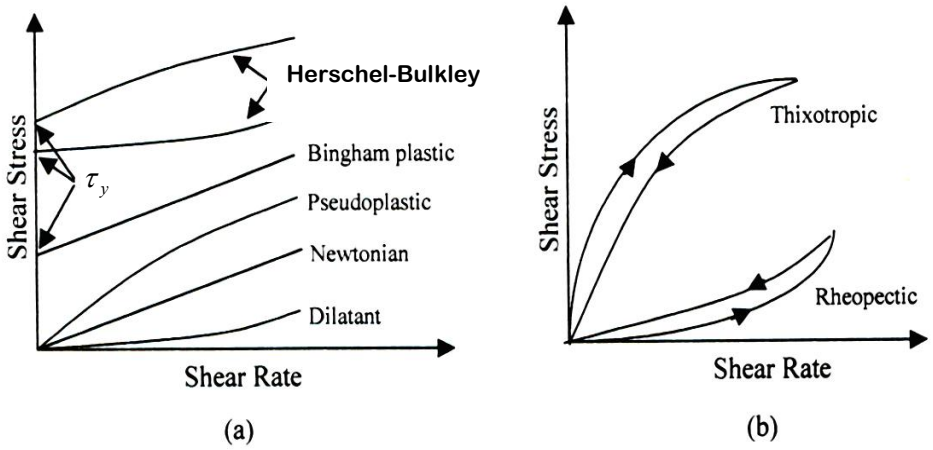

Figure 3.1 Flow curves of purely viscous non-Newtonian fluids.
(a) time-independent, and (b) time-dependent

In purely time-dependent fluids, the shear stress and fluid viscosity depend not only on the shear rate but also on the shear time the fluid experienced. Figure 3.1 (b) shows two types of time-dependent flow curves. At a given shear rate, the shear stress of thixotropic fluid decreases with the time period of shearing, while, for a rheopectic fluid, it increases.

In viscoelastic fluids, material possesses both elastic and viscous properties. They may show partial elastic recovery after deformation.

It is noteworthy to mention that the fluid biomaterials used in scaffold fabrication are usually either time-independent or time-dependent materials. The current research will only focus on the time-independent flow behaviour.

3.2 Modelling the Time-independent non-Newtonian Flow Behaviour

In the literature [Wilkinson, 1960; Skelland, 1967; Barns, 1989; Chhabra and Richardson, 1999], there are many empirical equations to describe the time-independent non-Newtonian flow behaviour. The equation selected for this research should not only represent the nonlinear flow curves but also be convenient to be integrated in the model development. The "Generalized power law" equation is one of such equations, in which the shear stress *vs.* shear rate relationship is represented by:

$$\tau = \eta(\dot{\gamma}) \cdot \dot{\gamma} = \tau_y + K\dot{\gamma}^n \tag{3.1}$$

where τ and τ_y are the shear stress and yield stress in flow, respectively; $\dot{\gamma}$ is the shear rate; K the consistency index, and n the power law index. K is a measure of viscosity, i.e., the higher K, the more viscous the fluid is. n is a measure of the degree of non-Newtonian behaviour, i.e., the greater departure of n from unity, the more pronounced are the non-Newtonian behaviour of the fluid material.

This model is a generalized model for time-independent non-Newtonian fluids. It can be used to represent various fluids showed in Figure 3.1(a) if *K, n* and τ_y are given different values. Particularly,

- For Newtonian fluid: $\tau_y = 0$, $n = 1$, K is the absolute fluid viscosity.
- For Dilatant and Pseudoplastic fluid: $\tau_y = 0$, $n \neq 1$.
- For Bingham plastic fluid: $\tau_y \neq 0$, $n = 1$.
- For Herschel-Bulkley fluid: $\tau_y \neq 0$, $n \neq 1$.

3.3 Experimental Method and Instrument

In the context of fluid dispensing, there are two different methods for determination of fluid parameters associated with non-Newtonian flow behaviour. One is the conventional method by using a rheometer. The other one, inspired by the idea of system identification, determines the fluid parameters directly from a few dispensing experiments [Chen and Ke, 2006]. In this chapter, the conventional method is used, while the other method is presented in detail in Chapter 6.

The instrument used in the experiment is a Brookfield DV-III Ultra Programmable Rheometer (Brookfield Engineering Lab., Inc., MA, USA), shown in Figure 3.2. The spindle geometry consists of a flat plate and a rotating cone, whose apex barely touched the plate surface. The structure is shown schematically in Figure 3.3. Temperature control is applied to the

lower plate. A sample of fluid is sheared in the narrow gap between the cone and plate. To maintain the fluid sample sheared at a constant rate, the obtuse angle on the cone is designed to be very small.

The measurement of the rheometer is based on the summation of the torque on the cone surface as a function of the angular velocity, from which the flow curves of the shear stress *vs.* shear rate are generated. The model parameters, i.e. τ_y, K and n in Eq. (3.1), are then identified through curve fitting.

Based on the structure of the cone-plate spindle shown in Figure 3.3, the following equations are used to calculate the shear stress, shear rate, and viscosity [Panton, 1996; White, 2003].

$$\text{Shear stress (N/m}^2\text{):} \qquad \tau = \frac{3T}{2\pi r^3} \tag{3.2}$$

$$\text{Shear rate (sec}^{-1}\text{):} \qquad \dot{\gamma} = \frac{\omega}{\sin\theta} \tag{3.3}$$

$$\text{Fluid viscosity (poise):} \qquad \eta = \frac{\tau}{\dot{\gamma}} \tag{3.4}$$

where T is the measured torque on the cone, r the cone radius, θ the cone obtuse angle, and ω the angular velocity of the cone.

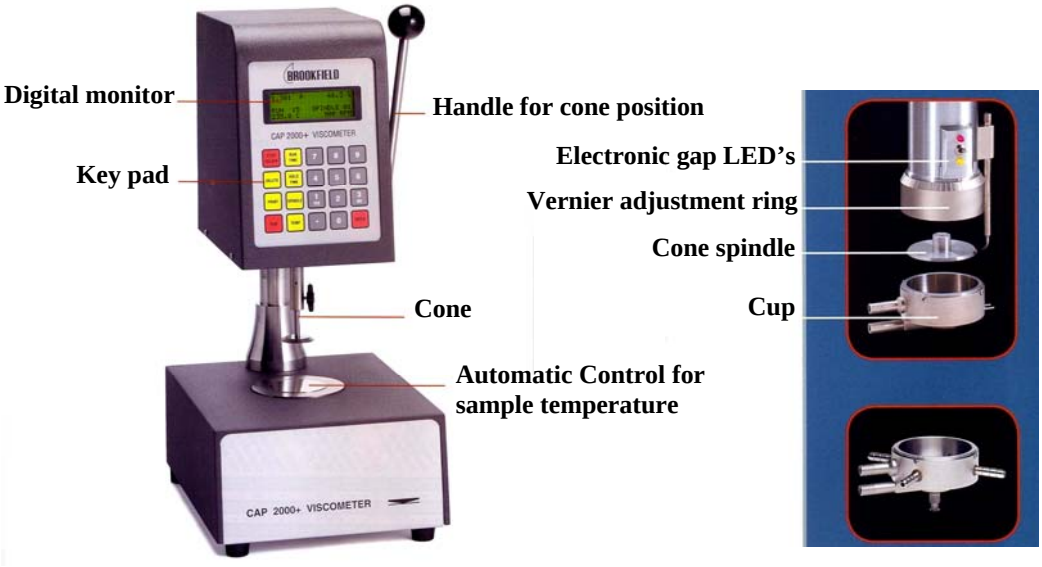

Figure 3.2 DV-III Ultra Programmable Rheometer provided by Brookfield Engineering Lab. Inc., MA, USA; (a) overview, and (b) cone-plate sample cup.

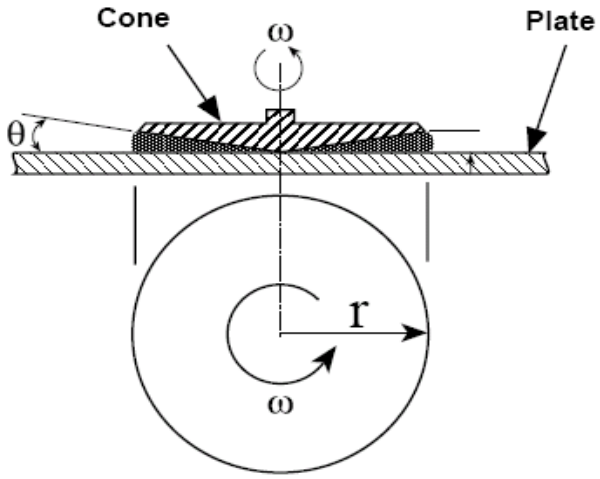

Figure 3.3 Structure of the cone-plate spindle of rheometer

3.4 Experimental Result and Discussion

Using the rheometer described above, the flow curves of the 2% (w/v) solution of chitosan in 0.2 mol/L acetic acid were measured at different temperatures. The relationship of shear stress *vs.* shear rate is shown in Figure 3.4(a). To avoid the possible influence of the shearing time, the shear rate was scanned quickly in each measurement, and a break with a relatively long time period (15 min) was set between two measurements. The fluid viscosity determined by $\eta = \tau / \dot{\gamma}$ is shown in Figure 3.4(b). It can be seen that the fluid viscosity decreases with an increased shear rate. The viscosity curves were fit mathematically by using the following equation, which is derived from Eq. (3.1):

$$\eta(\dot{\gamma}) = \frac{\tau}{\dot{\gamma}} = \frac{\tau_y}{\dot{\gamma}} + K\dot{\gamma}^{n-1} \tag{3.5}$$

where τ_y, K and n are measures of the yield stress, the fluid viscosity, and the degree of non-Newtonian flow behaviour, respectively, which have been stated before in Eq. (3.1).

After curve-fitting, τ_y and n are given the constant value of $\tau_y = 0$, $n = 0.89$, respectively; and K is decreasing with an increase of temperature, as illustrated in Figure 3.5. In this study, K was correlated with temperature by using the following exponential function:

$$K = K_0 e^{-\frac{T}{\lambda}} \tag{3.6}$$

where T is the temperature; K_0 and λ are curve-fitting parameters, whose values are given by $K_0 = 2824\ \text{cP}\cdot\text{s}^n$, $\lambda = 25.42\ ^{\circ}\text{C}$.

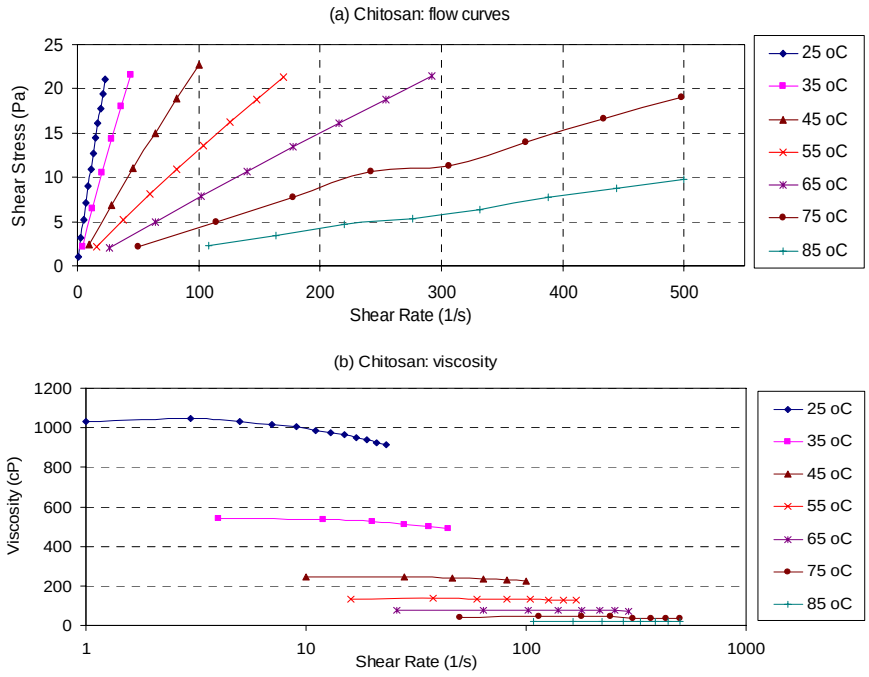

Figure 3.4 Non-Newtonian flow behaviour of chitosan solution; (a) flow curves at different temperatures and (b) fluid viscosity; it varies at different

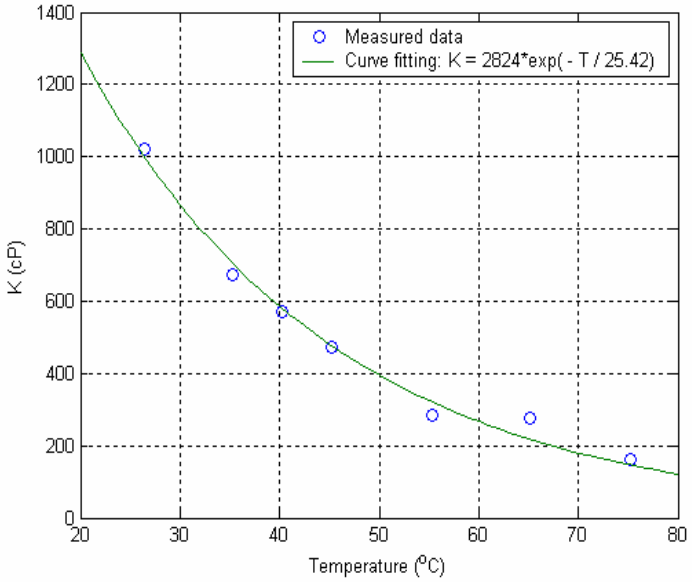

Figure 3.5 Dependency of *K* on temperatures

3.5 Summary

The non-Newtonian flow behaviour of scaffold biomaterials was introduced briefly in this chapter. By using a typical commercial rheometer, experiments were conducted to measure and characterize the flow behaviour of chitosan solution (2% w/v) in acetic acid. The results showed that the fluid viscosity and shear stress are dependent on the shear rate and temperature. Fluid parameters associated with non-Newtonian flow behaviour were then determined and identified by means of curve-fitting based on the experimental data.

CHAPTER 4

MODELLING OF THE FLOW RATE OF BIOMATERIALS DISPENSED

4.1 Introduction

Dispensing-based rapid prototyping (RP) technique has been widely used in the fabrication of tissue scaffolds [Philbrook, 1996; Bredt, 1998; Landers, 2000; Hutmacher, 2001]. As mentioned in Chapter 1, a key procedure in the RP fabrication process is the dispensing of fluid biomaterials. The flow rate of the dispensed fluid is an important index of the fabrication process, because it will determine the size (i.e., the height, width, and area) of the cross-section of coagulated strands, thus affecting the properties of tissue scaffolds [Freed, 1994; Hutmacher, 2001; Landers, 2002; Fang, 2005]. In this chapter, a model is developed to represent the flow rate of the dispensed biomaterials in the scaffold fabrication process.

4.2 Model Development for the Flow Rate of Biomaterials Dispensed

A typical dispensing system used for tissue scaffold fabrication is schematically shown in Figure 4.1, which was once described in Chapter 1.

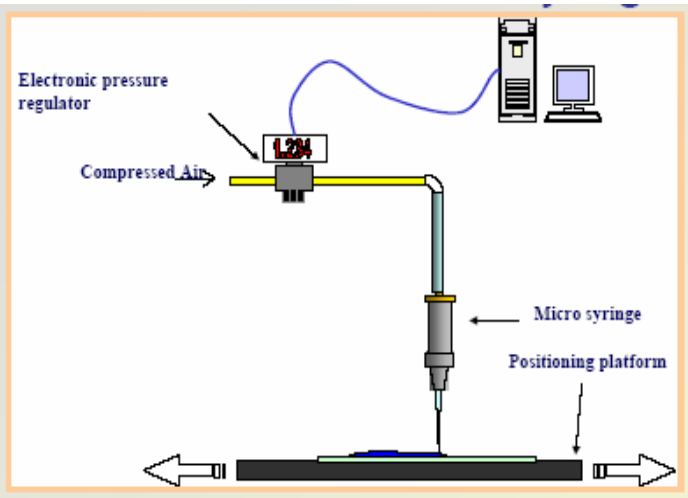

(a) Overview of the dispensing system

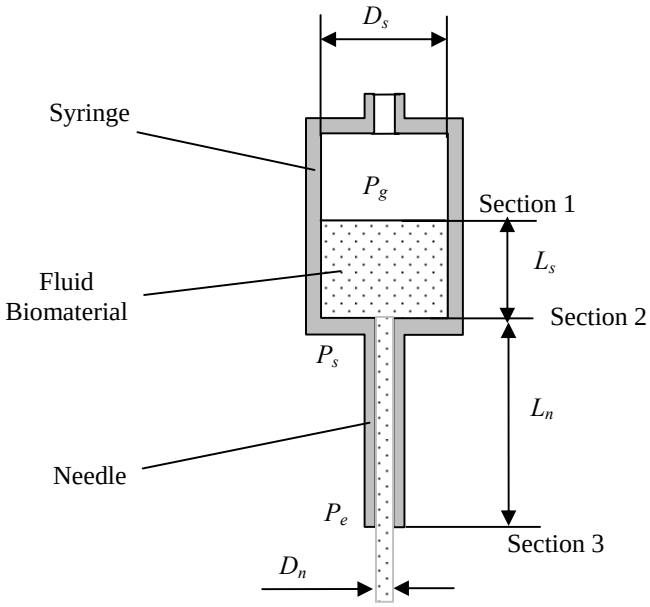

(b) Structure of the dispenser

Figure 4.1 Typical dispensing system used in the tissue scaffold fabrication

In this figure, P_g is the air driving pressure; P_e and P_s denote the fluid pressures at the needle and the syringe outlet, respectively. Other symbols represent geometries of the dispenser head. In the tissue scaffold fabrication, it is assumed for the dispensing process that:

(1) the fluid biomaterial is incompressible and time-independent.

(2) the flow in the syringe and needle is steady, laminar, and axisymmetric flow.

(3) there is no slip of fluid biomaterials on the wall of syringe and the needle.

(4) the needle diameter is much smaller than that of the syringe.

These assumptions are reasonable and closely approximate the real fabrication process.

4.2.1 Flow in the Syringe (between section 1 and 2)

By means of Bernoulli equation [White, 2003], the relationship between the air driving pressure, P_g, and the fluid pressure at the outlet of syringe, P_s, is given by:

$$\frac{P_g}{\rho g} + L_s + \alpha_1 \frac{v_1^2}{2g} = \frac{P_s}{\rho g} + \alpha_2 \frac{v_2^2}{2g} + \sum h \tag{4.1}$$

where $v_1(v_2)$ and $\alpha_1(\alpha_2)$ are the average velocity of flow and the kinetic energy correction factor, respectively, at section 1 (section 2); ρ is the density of the fluid biomaterial, g the

gravitational acceleration, and $\sum h$ the sum of the pressure drops between section 1 and 2. Pressure drops are derived from the friction loss and entrance loss in the flow, and calculated by:

$$\sum h = f\frac{L_s}{D_s}\frac{v_1^2}{2g} + K_c\frac{v_2^2}{2g} \tag{4.2}$$

where f is the Darcy friction factor and K_c the entrance loss correction factor.

Based on assumption (4), the term of $v_1^2/2g$ can be ignored as that $v_1 << v_2$. Thus the air driving pressure is derived and given by:

$$P_g = P_s - \rho g L_s + \rho v_2^2\frac{\alpha_2 + K_c}{2} \tag{4.3}$$

For the scaffold biomaterials with non-Newtonian flow behaviour, the evaluation of the kinetic energy correction factor, α, and the entrance loss correction factor, K_c, is very difficult and not well defined in literature. Some measurements of non-Newtonian fluids [Bogue, 1959] indicated that the combined correction for kinetic energy effect and entrance effect is the same as that of Newtonian fluids, in which the value of α is 2.0 for laminar flow and K_c is suggested as 0.23 for a slightly rounded entrance [Foust, 1960]. Thus the driving pressure of air is calculated by:

$$P_g = P_s - \rho g L_s + 1.115\rho v_2^2 \tag{4.4}$$

4.2.2 Flow in the Needle (between section 2 and 3)

The fundamental equations of fluid mechanics are used to describe the laminar flow in the needle, which is governed by the continuity and Navier-Stokes equation [Panton, 1996; White, 2003]:

Continuity equation: $\nabla \cdot v = 0$

Navier-Stokes equation (in cylinder coordination system):

$$\frac{\partial \rho}{\partial t} + \frac{1}{r}\frac{\partial}{\partial r}(\rho r v_r) + \frac{1}{r}\frac{\partial}{\partial \theta}(\rho v_\theta) + \frac{\partial}{\partial z}(\rho v_z) = 0 \tag{4.5}$$

$$\rho\left(\frac{\partial v_r}{\partial t} + v_r\frac{\partial v_r}{\partial r} + \frac{v_\theta}{r}\frac{\partial v_r}{\partial \theta} - \frac{v_\theta^2}{r} + v_z\frac{\partial v_r}{\partial z}\right) = \left[\frac{1}{r}\frac{\partial}{\partial r}(r\tau_{rr}) + \frac{1}{r}\frac{\partial}{\partial \theta}\tau_{\theta r} + \frac{\partial}{\partial z}\tau_{zr} - \frac{\tau_{\theta\theta}}{r}\right] - \frac{\partial P}{\partial r} \tag{4.6a}$$

$$\rho\left(\frac{\partial v_\theta}{\partial t} + v_r\frac{\partial v_\theta}{\partial r} + \frac{v_\theta}{r}\frac{\partial v_\theta}{\partial \theta} + \frac{v_r v_\theta}{r} + v_z\frac{\partial v_\theta}{\partial z}\right) = \left[\frac{1}{r^2}\frac{\partial}{\partial r}(r^2\tau_{r\theta}) + \frac{1}{r}\frac{\partial}{\partial \theta}\tau_{\theta\theta} + \frac{\partial}{\partial z}\tau_{z\theta} + \frac{\tau_{\theta r} - \tau_{r\theta}}{r}\right] - \frac{1}{r}\frac{\partial P}{\partial \theta} \tag{4.6b}$$

$$\rho\left(\frac{\partial v_z}{\partial t} + v_r\frac{\partial v_z}{\partial r} + \frac{v_\theta}{r}\frac{\partial v_z}{\partial \theta} + v_z\frac{\partial v_z}{\partial z}\right) = \left[\frac{1}{r}\frac{\partial}{\partial r}(r\tau_{rz}) + \frac{1}{r}\frac{\partial}{\partial \theta}\tau_{\theta z} + \frac{\partial}{\partial z}\tau_{zz}\right] - \frac{\partial P}{\partial z} + \rho g \tag{4.6c}$$

where τ_{ij} $(i, j = r, \theta, z)$ is the shear stress tensor.

Under assumption (2) that the flow in the needle is steady, incompressible and axisymmetric flow, Eq. (4.5) is reduced to

$$\frac{1}{r}\frac{\partial}{\partial r}(\rho r v_r) = 0 \tag{4.7}$$

Because there is no flow penetrating the needle wall, the boundary condition is $v_r\big|_{r=D_n/2}=0$, then v_r is equal to zero everywhere in the needle. The only velocity component is v_z and it is related to radius *r*, i.e.,

$$v_z = v_z(r) \tag{4.8}$$

Thus, from Eq. (4.6a) and Eq. (4.6b), it is known that the pressure gradients in the directions of *r* and θ are all zeros. Meanwhile, from Eq. (4.6c) the pressure gradient in the *z* direction is given by

$$\frac{dP}{dz} = \frac{P_e - P_s}{L_n} = \frac{1}{r}\frac{\partial}{\partial r}(r\tau) + \rho g \tag{4.9}$$

where τ is the shear stress in the fluid and given by:

$$\tau_{rz} = \left(\frac{P_e - P_s - \rho g L_n}{2L_n}\right)r = -\frac{\Delta P_n}{2L_n}r \tag{4.10}$$

where ΔP_n (i.e., $\Delta P_n = P_s + \rho g L_n - P_e$) is the pressure drop in the needle.

According to Eq. (4.10), the shear stress at the needle wall ($r = \frac{D_n}{2}$) is:

$$\tau_w = \frac{\Delta P_n}{2L_n}\cdot\frac{D_n}{2} \tag{4.11}$$

In Eq. (4.9) and (4.10), P_e is the pressure of the fluid biomaterials at the outlet of the needle. It should be noted that the fluid pressure, P_e, is not equal to the ambient air pressure if the fluid surface tension of biomaterials is considered. Fluid surface tension, one of the most important properties of fluid materials, is resulted from the attractive force between adjacent molecules. It points in a tangent direction along the air/fluid surface contour, acting like a stretched membrane on the fluid [Panton, 1996; White, 2003]. The effect of surface tension is illustrated in Figure 4.2. The resultant force due to the surface tension is balanced by the pressure difference between the fluid inside and the ambient air, i.e.

$$(P_e - P_0)L \cdot D_n = 2L\sigma \quad \text{or} \quad P_e = P_0 + \frac{2\sigma}{D_n} \tag{4.12}$$

where P_0 is the ambient air pressure, σ the surface tension of fluid biomaterials, and D_n the diameter of the needle. In the scaffold fabrication, D_n is usually very small, typically in the range of 200-500 μm. Therefore, the effect of fluid surface tension has significant influence on the fluid pressure, P_e.

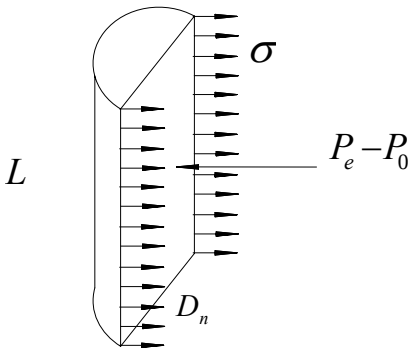

Figure 4.2 Fluid surface tension

As discussed earlier, the flow concerned is one dimensional, therefore the shear rate can be depicted into a simple expression, i.e.,

$$\dot{\gamma} = \dot{\gamma}_{rz} = \frac{\partial v_r}{\partial z} + \frac{\partial v_z}{\partial r} = \frac{dv_z}{dr} \tag{4.13}$$

Because of the yield shear stress τ_y, a threshold radius $r_c = \frac{2\tau_y L_n}{\Delta P_n}$ virtually exists in the needle: when $0 < r < r_c$ (i.e., $\tau_{rz} < \tau_y$), the shear rate, $\dot{\gamma}$, is zero. It means that there is no fluid deformation in this domain and the flow velocity is a constant (i.e., $\frac{dv_z}{dr} = 0$). For $r_c \le r < \frac{D_n}{2}$ (i.e., $\tau_{rz} \ge \tau_y$), the shear stress can be expressed by a generalized power equation, which is the same as Eq. (3.1), i.e.

$$\tau = \tau_{rz} = \frac{\Delta P_n}{2L_n} r = \tau_y + K\left(\frac{dv_z}{dr}\right)^n = \tau_y + K\dot{\gamma}^n \tag{4.14}$$

4.2.3 Flow Rate of the Dispensed Biomaterial

Based on assumption (3) of that there is no slip at the needle wall, the velocity distribution of the flow in the needle can be derived from Eq. (4.14).

When $0 < r < r_c$ ($\tau_{rz} < \tau_y$), the velocity is a constant:

$$v_z = \frac{2L_n}{\Delta P_n}\frac{n}{n+1}\frac{1}{K^{1/n}}(\tau_w - \tau_y)^{\frac{n+1}{n}} = \text{Constant} \tag{4.15a}$$

When $r_c \le r < \frac{D_n}{2}$ ($\tau_{rz} \ge \tau_y$), the flow velocity is calculated by:

$$v_z(r) = \frac{2L_n}{\Delta P_n}\frac{n}{n+1}\frac{1}{K^{1/n}}[(\tau_w - \tau_y)^{\frac{n+1}{n}} - (\frac{\Delta P_n}{2L_n}r - \tau_y)^{\frac{n+1}{n}}] \tag{4.15b}$$

where r_c is the threshold radius of $r_c = \frac{2\tau_y L_n}{\Delta P_n}$, and τ_w is the shear stress on the needle wall (i.e., $\tau_w = \frac{\Delta P_n}{2L_n}\cdot\frac{D_n}{2}$).

The volume flow rate of fluid biomaterials can be derived from the integration of the velocity distribution function, which is given by

$$\begin{aligned} Q &= \int_0^{r_c} v_z 2\pi r dr + \int_{r_c}^{D_n/2} v_z(r) 2\pi r dr \\ &= \pi(\frac{D_n}{2})^3 n(\frac{\tau_w}{K})^{1/n}(1-\tau_y/\tau_w)^{\frac{n+1}{n}}\cdot[\frac{(1-\tau_y/\tau_w)^2}{3n+1} + \frac{2(\tau_y/\tau_w)(1-\tau_y/\tau_w)}{2n+1} + \frac{(\tau_y/\tau_w)^2}{n+1}] \end{aligned} \tag{4.16}$$

If the yield stress of the fluid biomaterial is very small ($\tau_y = 0$ for the chitosan solution as examined in Chapter 3), its influence on the flow rate can be ignored. Thus, the flow rate can be represented by the following equation, which is derived from Eq. (4.16),

$$Q = c(\Delta P_n)^{1/n} \tag{4.17}$$

where c is a coefficient and given by

$$c = \frac{\pi n D_n^{(3n+1)/n}}{2^{(3n+2)/n}(3n+1)(KL)^{1/n}} \tag{4.18}$$

It is noted that Eq. (4.17) is established for a needle with a uniform internal diameter. However, the case is always that the needle in a real dispensing system consists of two or more segments with different internal diameters, as shown in Fig. 4.3. In such a case, Eq. (4.17) can be used individually for each of the segments. The previous study [Chen, 2006] indicated that it is also applicable to use an equivalent coefficient c in Eq. (4.17), in which

$$c = \left(\frac{1}{\frac{1}{c_1^n} + \frac{1}{c_2^n} + \cdots + \frac{1}{c_m^n}} \right)^{1/n} \tag{4.19}$$

where c_1, c_2, … and c_m are the coefficients associated with individual segments, each of which is evaluated by using Eq. (4.18) with the diameter and length replaced correspondingly.

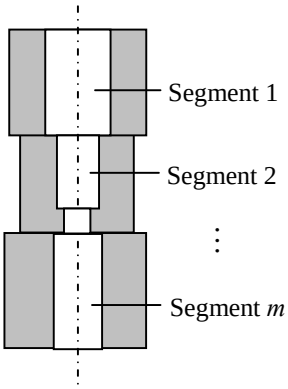

Figure 4.3 Dispenser needle consisting of *m* segments with different diameters

4.3 Experimental Verification

4.3.1 Experiments and Result

To verify the effectiveness of the developed model, experiments were carried out by using a typical commercial automated fluid dispensing system (C-720, Asymtek, USA). Figure 4.4 shows this system: (a) is the overview of the dispensing system, and (b) is the close-up view of the dispenser head. The dispenser head can be controlled to move in three directions; and the temperature of the needle is ensured by a mounted needle heater with a resolution of $\pm 1^{o}$C. In the experiments, the temperatures at the syringe outlet, needle heater, and needle were monitored respectively by using thermocouples. The values of the related geometries of the dispenser head are listed in Table 4.1.

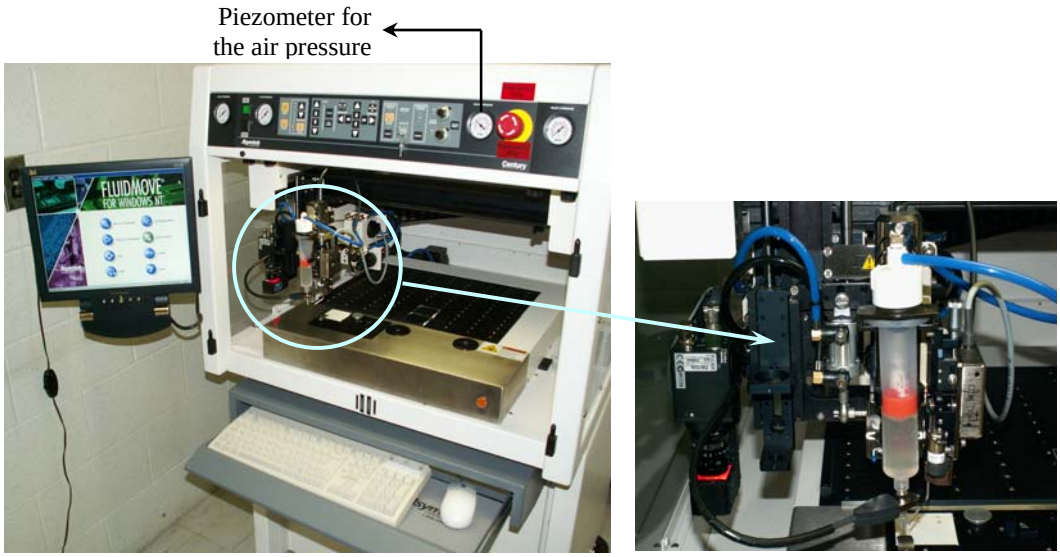

(a) (b)

Figure 4.4 Asymtek C-720 automated fluid dispensing system:
(a) overview of the dispensing system, and (b) close-up view of the dispenser head.

Table 4.1 Geometrical parameters of dispenser head

Parameters	**Values**
Needle internal diameter× length	0.20×18.0 mm
Needle heater internal diameter× length	2.32×18.55 mm
Syringe outlet internal diameter × length	2.32×10.0 mm

In the experiments, the chitosan solution (2% w/v) in acetic acid, the same material used in Chapter 2 and 3, was chosen for dispensing, and the dispensing system was controlled to deliver the solution for a time period of 30 seconds under different dispensing conditions. In each of the dispensing experiments, the average flow rate was measured by weighing the fluid dispensed with a build-in electronic balance. The measured flow rates and the corresponding

dispensing conditions are listed in Table 4.2. Meanwhile, the measurement of temperatures at the syringe outlet, needle heater, and needle is given in Table 4.3 when the temperature settings on dispenser head are 25°C, 35°C, 50°C, and 65°C, respectively.

Table 4.2 Measured flow rates under different dispensing conditions.

Measured flow rate (mg/s)		Applied air pressure (KPa)				
		50	100	150	200	250
Temperature (°C)	25	-	1.203	2.327	4.890	8.498
	35	0.347	1.342	3.256	6.163	9.822
	50	0.467	1.988	4.841	8.764	13.76
	65	0.554	2.847	6.633	11.251	17.162

Table 4.3 Measured temperatures at the syringe outlet, needle heater, and needle.

Temperature settings of the dispensing system (°C)	Measured temperatures (°C)		
	Syringe outlet	Needle heater	Needle
25	25.0	25.0	25.0
35	28.2	35.1	30.6
50	30.8	46.7	35.8
65	32.8	58.2	40.4

4.3.2 Model Prediction

Based on the model developed in this chapter, i.e., Equations (4.16) - (4.19), simulations to predict the flow rate of the chitosan solution dispensed were performed in MatLab. In the simulation, the fluid parameters, which are summarized in Table 4.4, were cited from the

previous rheometer measurement. The predicted flow rates are shown in Figure 4.5 (a-d) for the temperature settings of 25°C, 35°C, 50°C, and 65°C, respectively. For comparison, the experimental result given in Table 4.2 is also presented in Figure 4.5.

Table 4.4 Parameters in non-Newtonian flow behaviour of the chitosan solution, identified by using a rheometer

Generalized power law equation: $\tau = \tau_y + K\dot{\gamma}^n$			
τ_y	n	$K = K_0 e^{-T/\lambda}$	
		K_0 (cP)	λ (°C)
0	0.89	2824	25.42

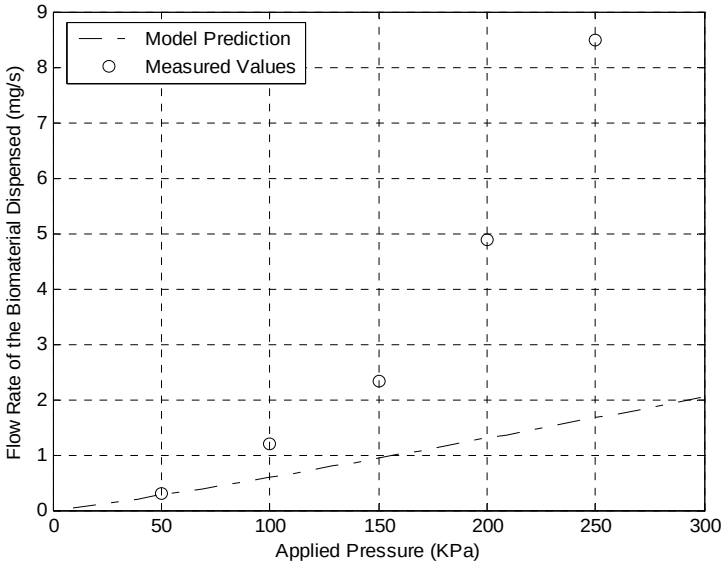

(a) Temperature of the dispensing system is set at 25 °C

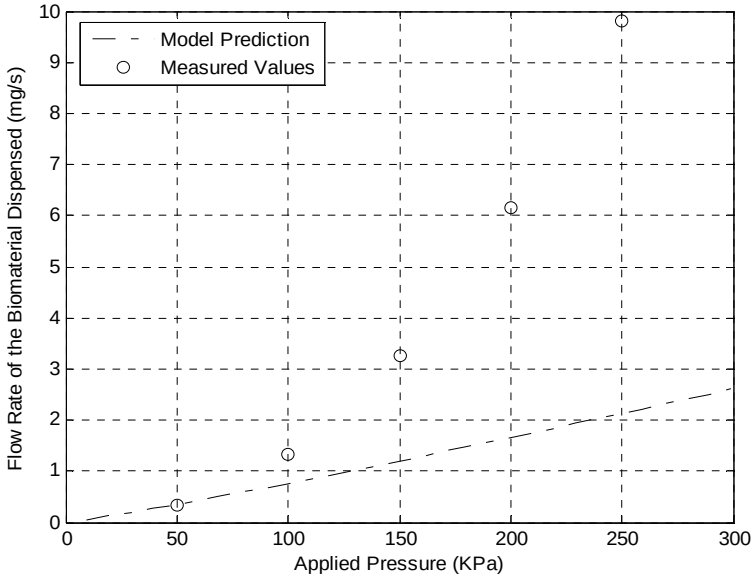

(b) Temperature of the dispensing system is set at 35 ^{o}C

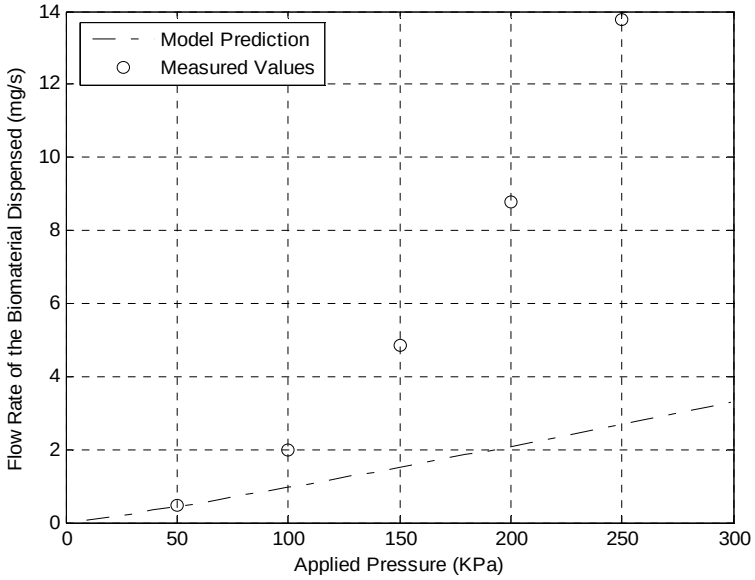

(c) Temperature of the dispensing system is set at 50 ^{o}C

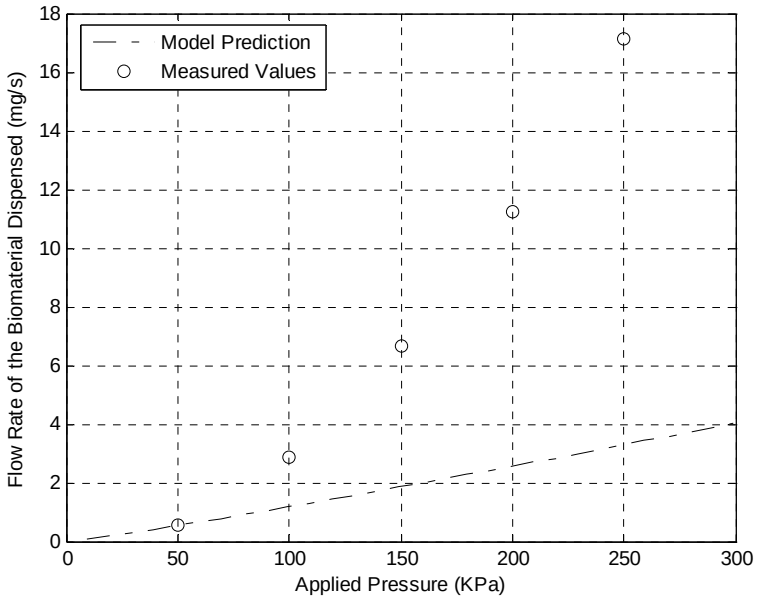

(d) Temperature of the dispensing system is set at 65 ^{o}C

Figure 4.5 Comparison between the measured flow rates and the model predictions, in which the flow behaviour is identified by rheometer.

From the comparison given in Fig 4.5, it can be seen that there is relatively large difference between the simulation results and the experimental ones. This discrepancy is considered mainly to be resulted from the temperature difference between the dispensing system and the rheometer used for the flow behavior identification in the preceding chapter. It is a fact that the temperatures of the dispensing system and the rheometer were manipulated by different control systems in this study. Due to the sensitivity of flow behaviour to temperature, the model simulations require that fluid properties be identified by the rheometer at temperatures exactly the same as those actually in the dispenser head. Otherwise, a little difference between them can result in a large error in the model predictions, as shown in Figure 4.5.

To alleviate the above problem, another method was proposed and used in this study. Instead of using a rheometer, the flow behaviour of the chitosan solution was identified and characterized directly from the experimental dispensing result. Specifically, some of the experimental data were chosen for the flow behaviour characterization, and the others could be used to verify the simulation result. For this purpose, the shaded data of measured flow rates, as shown in Table 4.2, were used to identify the flow behaviour of chitosan solution dispensed. It is suggested that the chosen data should cover the whole range of dispensing conditions, namely, all levels of applied air pressure and temperatures used in experiments.

Based on the developed models of Eq. (4.16) to (4.19), fluid parameters associated with the non-Newtonian flow behaviour, i.e., n, K_0, and λ in Table 4.4, were identified from the shaded data in Table 4.2. In such a process, the function of non-linear least-squares data-fitting in MatLab was used, which will be introduced in more detail in Chapter 6. The estimated values of fluid parameters are given by $n = 0.475, K_0 = 48160$ cP, $\lambda = 42.91$ °C , respectively, for the chitosan solution dispensed. They are somewhat different from the ones listed in Table 4.4, which were identified by rheometer in the preceding chapter.

For the model verification, simulations to predict the flow rate of the chitosan solution dispensed were again performed in MatLab. However, the fluid parameters used in these simulations were identified from the dispensing experiments (as discussed above), rather than from the rheometer. The predicted flow rates are shown in Figure 4.6 (a-d), with a legend of *Model Prediction II*, for the temperature settings of 25°C, 35°C, 50°C, and 65°C, respectively. For comparison, the experimental results in Table 4.2 and the previous model predictions in Figure 4.5 (with a legend of *Model Prediction I*) are also presented in Figure 4.6.

From the comparison, it can be seen that the model developed in this study, combined with the method of identifying the flow behaviour from dispensing results, is very promising to predict the flow rate in the scaffold fabrication process. The difference between the experimental result and simulations are likely due to factors such as measurement noise and the limited resolution of dispensing conditions, including the applied air pressure and needle heater temperature.

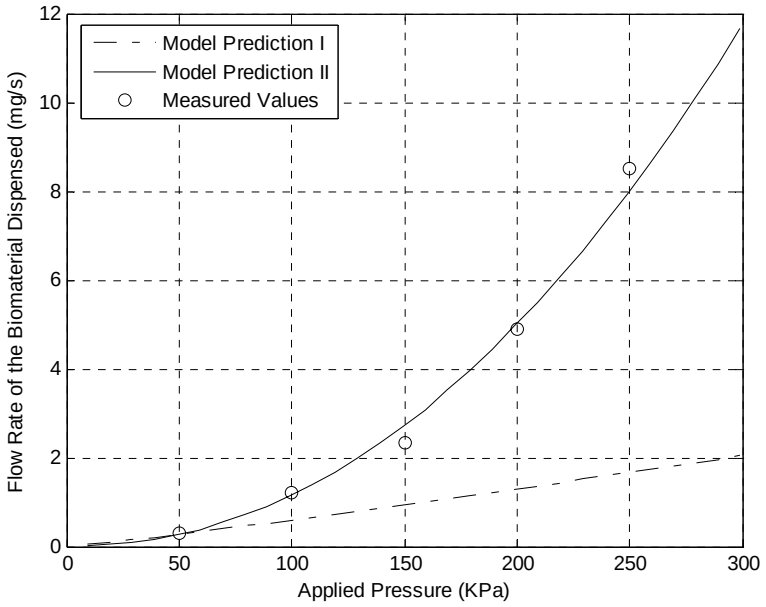

(a) Temperature of the dispensing system is set at 25 ^{o}C

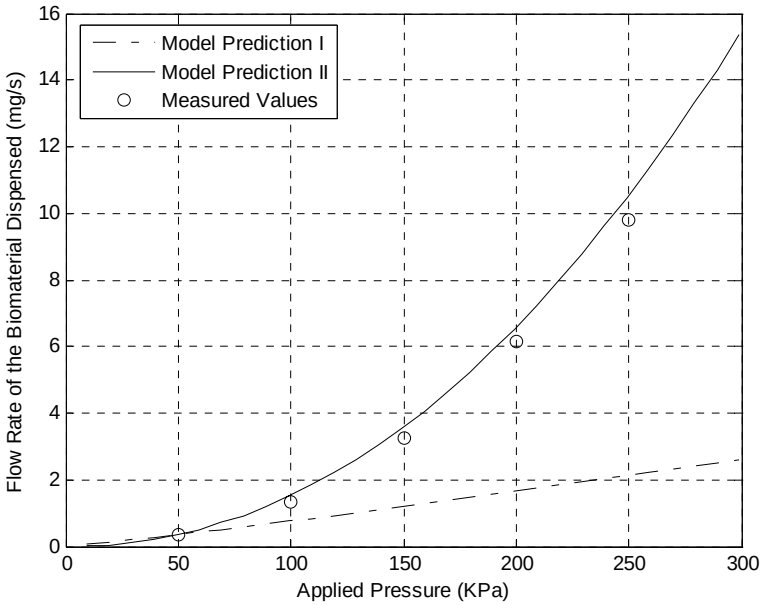

(b) Temperature of the dispensing system is set at 35 ^{o}C

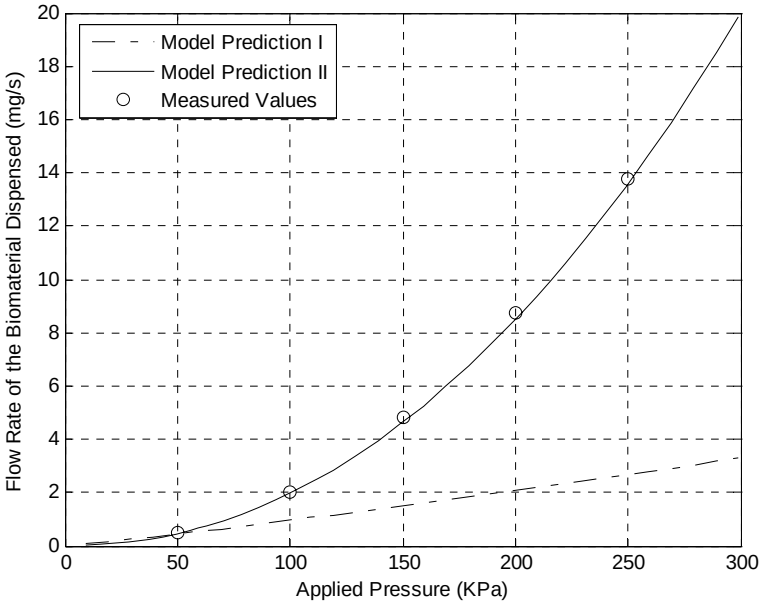

(c) Temperature of the dispensing system is set at 50 ^{o}C

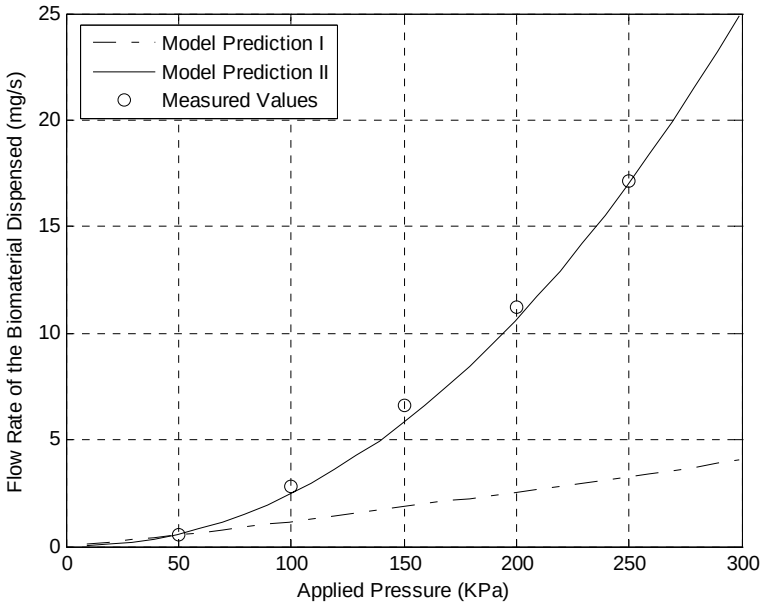

(d) Temperature of the dispensing system is set at 65 ^{o}C

Figure 4.6 Comparison between the measured flow rates and the model predictions. In *Model Prediction I*, the flow behaviour is identified by rheometer. In *Model Prediction II*, the flow behaviour is identified by dispensing results.

4.4 Summary

This chapter presented the development of a model to represent the flow rate of dispensed fluid biomaterials in the scaffold fabrication process. By using Bernoulli equation in fluid mechanics, the pressure drop along the dispenser syringe and needle is derived, with the consideration of pressure drops to overcome flow frictions along the wall and the entrance effect. The flow velocity distribution in the dispenser head is determined by using Navier-Stokes equation. Particularly, the surface tension of fluid was taken into account to identify the fluid pressure at the outlet of needle. After integration of the flow velocity along the needle diameter, a model to represent the flow rate of fluid biomaterials dispensed is developed.

To validate the developed model, experiments were carried out on a typical commercial automated fluid dispensing system (C-720, Asymtek, USA). The comparison of the experimental results to the model predictions, in which the flow behaviour is identified from rheometer, indicated that there was a relatively large difference between them. This is considered mainly resulting from the temperature difference between the dispensing system and the rheometer used for the flow behaviour identification. To alleviate the problem, a method was presented, in which the flow behaviour is identified from a few dispensing experiments rather than a rheometer. By using this method, the model predictions were improved a lot and in good agreement with the experimental results. This indicated that the developed model combined with this method is promising to predict the flow rate of dispensed biomaterials in scaffold fabrication process.

CHAPTER 5

MODELLING OF THE STRAND PROFILE AND SCAFFOLD POROSITY

5.1 Introduction

In the dispensing-based fabrication process of tissue scaffolds, the fluid biomaterial, once dispensed out of the needle, drops onto a substrate or the layer prototyped previously, spreading and finally coagulating into a strand. The profile and size (i.e., height, width, area) of the strand cross-sections are very important because they determine the pore size and interconnectivity, as well as the porosity of tissue scaffolds. Scaffold porosity represents the ratio of the volume of interconnected pores to that of the whole scaffold. It evaluates the relative space of interconnected network within the scaffolds for cell attachment, ingrowths, and tissue regeneration. It also significantly contributes to the mechanical properties of tissue scaffolds [Fang, 2005]. In this chapter, models are developed to represent the cross-sectional profile and porosity of tissue scaffolds.

5.2 Modelling the Profile of Strand Cross-sections

5.2.1 Equilibrium Profile of Cross-sections at Different Parts

Figure 5.1 shows the geometry of a scaffold considered in this study, which has a structure of square pattern ($0^o/90^o$). The cross-section of scaffold strands varies with the layer prototyped in the fabrication process. On the first layer, the strand profile is approximately a semi-oval cross-section, showed in Figure 5.1 (a); and for the subsequent layers, the portions (Part I in Figure 5.1) overlapped directly on the previous layer also have a semi-oval cross-section, while the portions (Part II in Figure 5.1) hung up between two strands have an oval cross-section, as shown in Figure 5.1 (b).

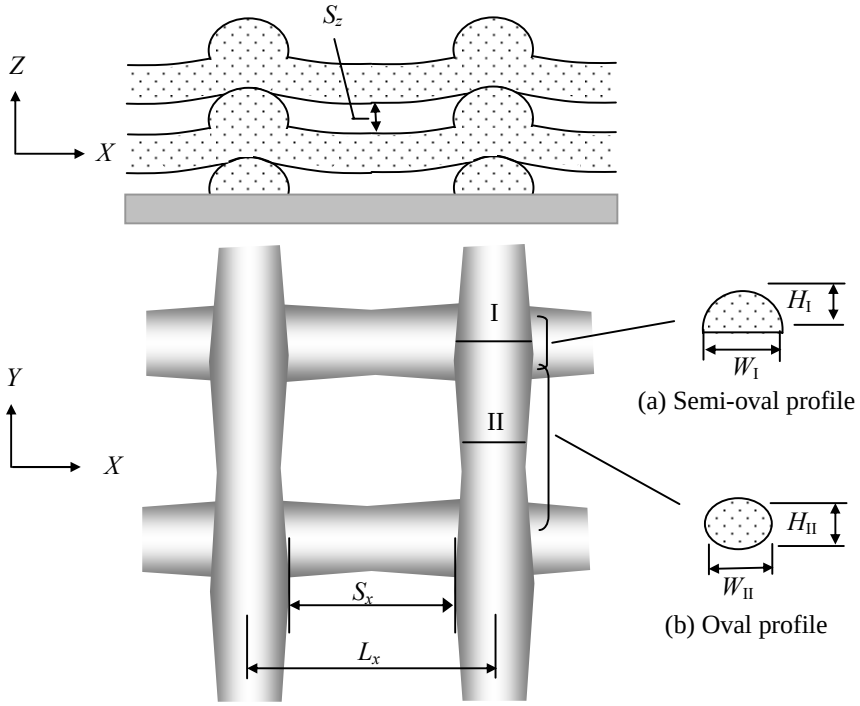

Figure 5.1 Geometry of a tissue scaffold with square pattern ($0^o/90^o$)

To represent the problem mathematically, the cross-sections of a scaffold strand, in both semi-oval and oval profile, are considered in a two-dimensional coordinate (x, z), as schematically showed in Figure 5.2, in which $h(x)$ denotes the interface between fluid biomaterials and the ambient air, and θ is the contact angle at the edge of the scaffold strand.

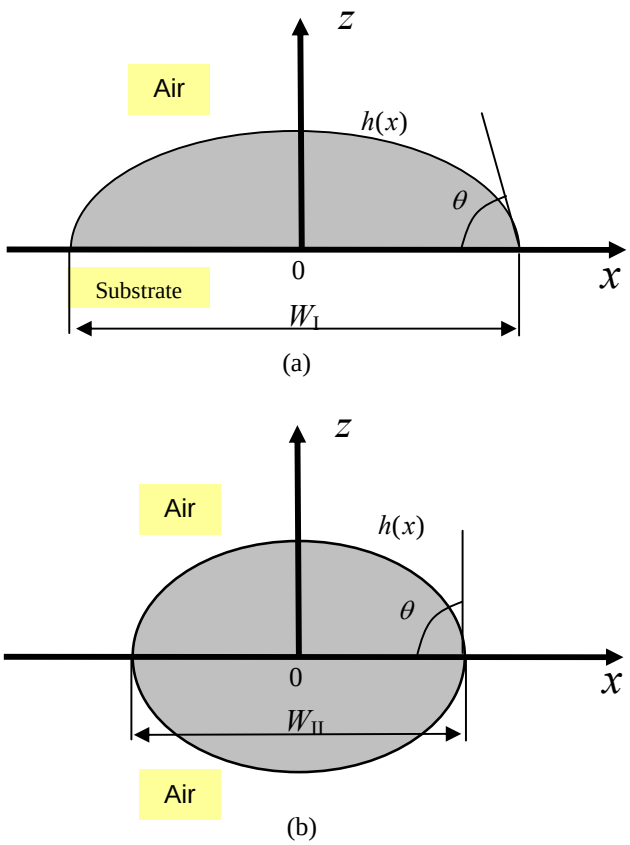

Figure 5.2 Cross-section of a scaffold strand with
(a) semi-oval profile and (b) oval profile

When a fluid material drops onto a solid surface, it is observed that it does not wet the surface but remains at an equilibrium shape having a definite angle of contact between the fluid and the surface. This angle is called the contact angle in fluid mechanics [Panton, 1996; White,

2003], shown as θ in Figure 5.2. The angle is affected by the surface chemistry of contacted materials and the ambient temperature [Han and Wang, 1997; Adamson and Gast, 1997]. Hundreds of years ago, Young first investigated this problem based on the surface tension between different material boundaries (air/fluid, fluid/board, and board/air). A comprehensive review of studies on contact angle and its influence on the spreading of fluids is provided by Adamson and Gast [1997], in which a common method to measure the contact angle is based on the scanning electron microscopy (SEM) analysis of the cross-section of spreading fluids. But it is limited by the experimental uncertainty and the repeatability.

The reason why contact angle is formed and the spreading of fluid materials reaches an equilibrium state is that the pressure difference across the curved interface is balanced by the effect of fluid surface tension. As mentioned in Chapter 4, the fluid surface tension arises from interactions between adjacent molecules, resulting in an attractive force along the air/fluid surface contour [Han and Wang, 1997; Adamson and Gast, 1997]. It is measured as the force exerted on a unit length of boundary contour of the fluid surface, with a dimension of N/m. The relationship between the pressure difference and the surface tension of fluid materials is represented by Young-Laplace equation [White, 2003] as:

$$\Delta p = \sigma\left(\frac{1}{R_1} + \frac{1}{R_2}\right) \tag{5.1}$$

where R_1 and R_2 are the principal curvature radii of the interface, Δp the pressure difference across the curved fluid/air interface.

For the tissue scaffold strands, the principle curvature radius is given by:

$$R_1 = \frac{(1+h'^2)^{3/2}}{h''}, \qquad R_2 = \infty \tag{5.2}$$

where h' and h'' denote the first and second derivatives of $h(x)$ with respect to x.

At the fluid/substrate interface, the fluid pressure is calculated by the height of strand cross-section:

$$P_{f-s} = P(x) = P + \rho g h \tag{5.3}$$

where P is the fluid pressure at the fluid/air interface. This pressure is not equal to the ambient air pressure, P_0, but related to the fluid surface tension of scaffold biomaterials. ρ is the fluid density, and h the height of strand cross-section, $h = h(x)$.

Thus along the curved fluid/air interface, the pressure difference, Δp, is a function of x and given by:

$$\Delta P = \Delta P(x) = P - P_0 = P_{f-s} - \rho g h - P_0 \tag{5.4}$$

Substituting Eq. (5.2), (5.4) into Eq. (5.1) yields:

$$\frac{P_{f-s} - \rho g h(x) - P_0}{\sigma} = \frac{h''}{(1+h'^2)^{3/2}} \tag{5.5}$$

The profile of the strand cross-section can be determined numerically from solving Eq. (5.5), combined with the boundary conditions given in the following section.

5.2.2 Boundary Conditions of the Spreading of Fluid Biomaterials

Once the spreading of fluid biomaterials reaches an equilibrium state, the following boundary conditions must be satisfied:

(1) There is no moving or spreading of fluid biomaterials.

$$\begin{aligned} v_x &= 0, \dot{v}_x = 0, \ddot{v}_x = 0 \\ v_y &= 0, \dot{v}_y = 0, \ddot{v}_y = 0 \end{aligned} \tag{5.6}$$

(2) Fluid biomaterial reaches the same temperature as the ambient air or environment.

$$T = T_0 \tag{5.7}$$

(3) Interface between the fluid biomaterial and the ambient air is symmetric and smooth.

$$h'(x=0) = \left.\frac{dh(x)}{dx}\right|_{x=0} = 0 \tag{5.8}$$

(4) Fluid biomaterial is assumed incompressible so that the volume is constant. On this basis, one has the following relationship, for the case of strand cross-section with an oval profile

$$Q = 2 \cdot V_n \cdot \int_{-W/2}^{W/2} h(x)dx \tag{5.9a}$$

and for strand cross-section with a semi-oval profile

$$Q = V_n \cdot \int_{-W/2}^{W/2} h(x)dx \tag{5.9b}$$

where Q is the flow rate of the fluid biomaterial dispensed, V_n the moving speed of the dispenser needle, W the width of the strand cross-section.

(5) At the edge of the strand cross-section, the slop angle of the tangent line is equal to the contact angle of fluid biomaterial, i.e.,

$$h'(x=\frac{W}{2})=-h'(x=-\frac{W}{2})=-\tan(\theta) \tag{5.10}$$

In the case of strand cross-section with an oval profile, the slop angle is 90^o under the assumption of symmetric fluid/air contour, i.e. $\theta=90^0$. For strand cross-section of semi-oval profile, the contact angle is related to the surface chemistry of materials and the temperature. The θ value can be determined experimentally by using scanning electron microscopy (SEM) analysis, as mentioned before.

5.3 Pore Size and Porosity of Tissue Scaffolds

For the scaffold showed in Figure 5.1, the pore size is denoted respectively by S_x in the X direction and S_z in the Z direction. If giving the distance between two strands (denoted by L_x in Figure 5.1), S_x and S_z can be determined by the strand profiles formed at Part I and Part II respectively. Based on the geometrical relation, one has

$$S_x = L_x - W_{\mathrm{I}} \tag{5.11}$$

$$S_z = 2H_{\mathrm{I}} - H_{\mathrm{II}} \tag{5.12}$$

where W_{I} (W_{II}) and H_{I} (H_{II}) are the width and height of strand cross-section at Part I (Part II) respectively. The values of W_{I}, W_{II}, H_{I}, and H_{II} can be determined by solving Eq. (5.5) with the corresponding boundary conditions discussed above.

The scaffold porosity can be developed based on the strand geometries. Assuming the scaffold structure pattern and the distance between strands have been specified in design, and there is no collapse due to the fusion between two layers, the volume percent (vol. %) porosity is defined as

$$\text{Vol.\% Porosity} = (1 - \frac{V_{strands}}{V_{scaffold}}) \times 100\% \tag{5.13}$$

where $V_{strands}$ is the volume of the strands, $V_{scaffold}$ the bulk volume of the fabricated scaffold. If the scaffold is designed into an interlacing structure of strand matrix with *l* rows, *m* columns, and *n* layers (i.e., $\text{row} \times \text{column} \times \text{layer} = l \times m \times n$), $V_{strands}$ and $V_{scaffold}$ can be evaluated by

$$V_{strand} = Q \cdot \frac{L_{strands}}{V_n} = Q \cdot \frac{l \cdot m \cdot n \cdot L_x}{V_n} \tag{5.14}$$

$$V_{scaffold} = l \cdot L_x \times m \cdot L_x \times n \cdot H_I \tag{5.15}$$

where $L_{strands}$ is the sum of strand length in the scaffold matrix, V_n the moving speed of the dispenser needle, L_x the pre-designed distance between two strands.

If the mass of the scaffold is measured, the volume of dispensed strands, $V_{strands}$, can also be evaluated from

$$V_{strand} = \frac{M_{scaffold}}{\rho} \tag{5.16}$$

where $M_{scaffold}$ is the mass of the scaffold and ρ the density of biomaterials.

Substituting Eq. (5.14), (5.15) into Eq. (5.13) yields

$$\text{Vol.\% Porosity} = (1 - \frac{V_{strands}}{V_{scaffold}}) \times 100\% = (1 - \frac{Q}{L_x \cdot H_I \cdot V_n}) \times 100\% \tag{5.17}$$

From the above equation, it can be seen that the volume porosity of tissue scaffolds is determined by the operation conditions of fabrication process, including the applied air driving pressure (to manipulate the flow rate, Q), the moving speed of dispenser needle (V_n), and the distance between two strands (L_x). Note that the height H_I is calculated from Eq. (5.5), which is also determined by Q and V_n.

5.4 Simulation Study

The performance of a dispensing-based fabrication process for tissue scaffolds is usually evaluated in terms of the flow rate of the fluid biomaterials, the profile of the strand cross-sections, and the scaffold porosity. The flow rate of dispensed biomaterials has been studied experimentally in Chapter 4. In this chapter, the strand cross-section profile and the scaffold porosity will be investigated by simulations. The objective is to identify the influence of different parameters on the dispensing-based fabrication process.

In tissue scaffold fabrication, the dispensing result is affected by many different parameters [Landers, 2002; Fang, 2005; Vozzi, 2002], which can be grouped into three categories:

(1) Operation parameters, which represent the operation conditions of the fabrication process, e.g. pressure (P_g), temperature (T) and moving speed (V_n) of the dispenser needle.

(2) Fluid parameters, which depict the properties of the biomaterial being dispensed, e.g. ρ, K, n, τ_y, the fluid surface tension, and the contact angle, etc.

(3) Structural parameters, which include the geometries of the dispenser head, e.g. D_n, D_s, L_n, L_s, etc.

To study the effect of different parameters on the fabrication process, the air driving pressure P_g (operation parameter), temperature T, which will affect the fluid viscosity (fluid parameter), and the needle diameter D_n (structural parameter) are chosen as test parameters and studied individually in the present study. The values of test parameters and other parameters are listed in Table 5.1. These values are used in all simulations in this chapter except where specified. The equilibrium profile of the strand cross-sections and the scaffold porosity are simulated in MatLab based on upon developed models showed in Eq. (5.5) and (5.17).

Table 5.1 Parameters used for simulations

Parameters	Values
Air driving pressure	P_g=102-132 kPa
Temperature	T=35 ^{o}C
Moving speed of dispenser needle	V_n=2.5 mm/s
Syringe diameter	D_s=50 mm
Needle diameter	D_n=200 μm
Needle length	L_n=18 mm
Fluid height in syringe	L_s=30 mm
Density of fluid biomaterial	ρ=1000 kg/m^3
Viscous consistency index	$K = K_0 e^{-T/\lambda}$
Curve-fitting parameters	$K_0 = 2824$ cP$\cdot$s^n, $\lambda = 25.42$ ^{o}C
Flow behaviour index	n=0.89
Yield stress	τ_y=0 Pa
Surface tension	σ =0.073 N/m
Ambiant air pressure	P_0=101.3 kPa

5.4.1 Effect of Air Driving Pressure

The effect of air driving pressure on the dispensing-based fabrication process was investigated by simulations; and the simulation results are given in Figure 5.3 (a-b). It can be seen that an increasing diving pressure results in an increase of width and height of the strand cross-section, and a decrease of scaffold porosity. The change pattern is nonlinear because of the nonlinear flow behaviour of fluid biomaterials, i.e., $n \neq 1$. As the air driving pressure increase, the pressure drop along the needle increase either, resulting in an increase in the flow rate of fluid biomaterials dispensed. Given a constant moving speed of the dispenser head, the area of

the strand cross-section will swell with the increasing flow rate. If the distance between two strands, L_x, is maintained a constant, the volume of the pores of tissue scaffolds will become smaller and the porosity decreases consequently. In a practical fabrication process, the magnitude of the air driving pressure should be controlled precisely to obtain the desired scaffold porosity and the size of interconnected pores.

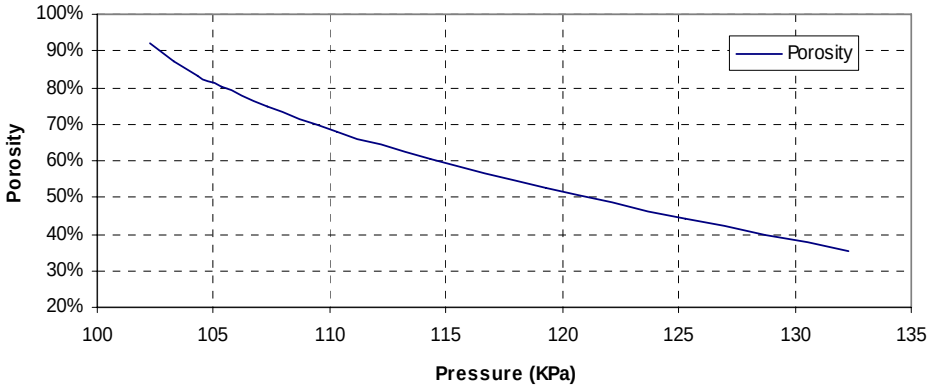

(a). Porosity *vs.* air driving pressure

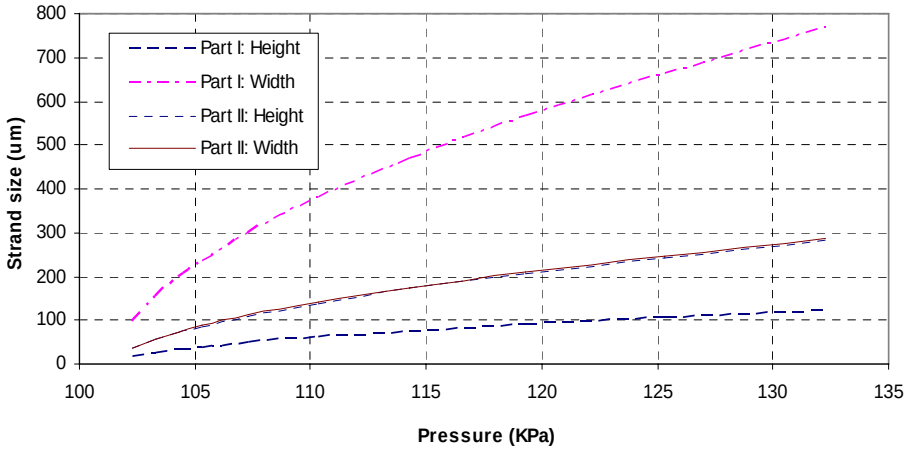

(b). Strand size *vs.* air driving pressure

Figure 5.3 Effect of air driving pressure, P_g

5.4.2 Effect of Temperature

The fluid properties are associated with the temperature of the dispenser head, thus the fabrication process is influenced. The effect of temperatures was evaluated by simulations, and the results are shown in Figure 5.4 (a-b).

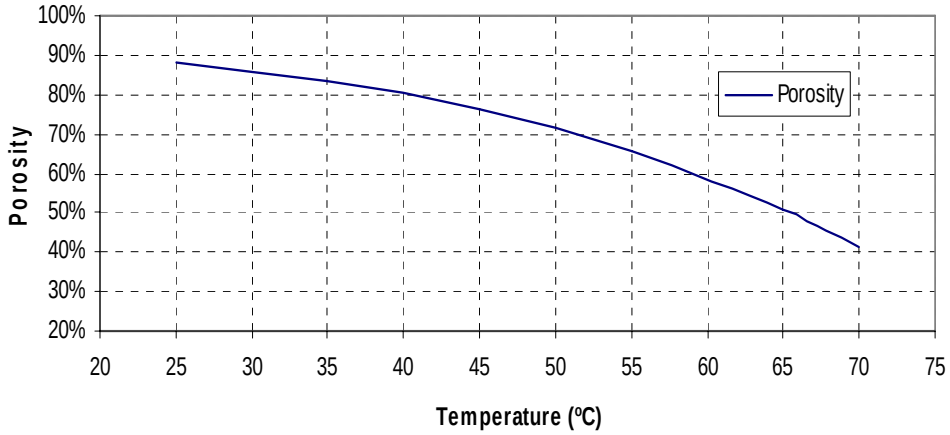

(a). Porosity *vs.* temperature

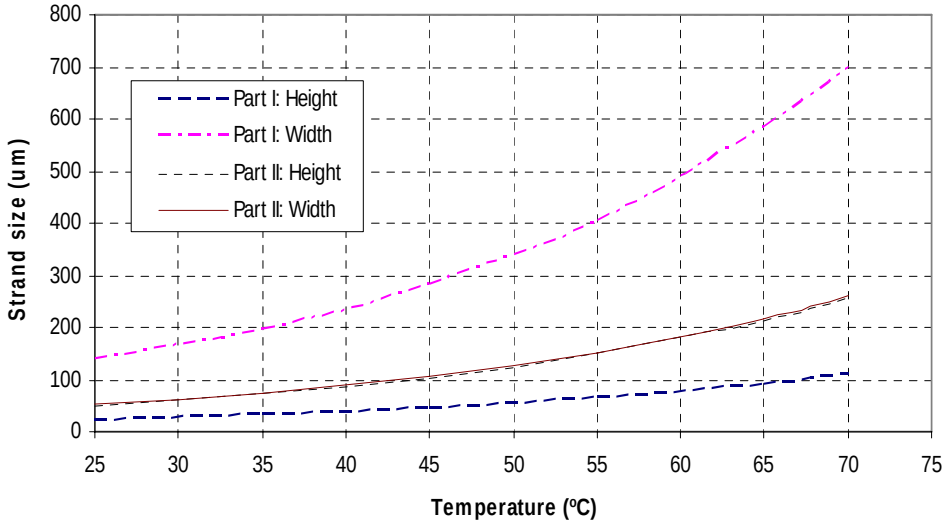

(b). Strand size *vs.* temperature

Figure 5.4 Effect of temperature, *T*

With an increasing temperature, the fluid viscosity will decrease by an exponential pattern as shown in Figure 3.5, thus resulting in an increase of flow rate and the size of strand cross-sections, as well as a decrease of scaffold porosity. By using developed models, the profile and size of strand cross-sections at Part I and II can be evaluated numerically. It can be seen that the size of strand cross-sections increase with an increasing temperature, but the width at Part I, W_{I}, is more sensitive than other parameters of the strand cross-sections. One of the interesting observations in the present study is that if $T < 45\,^{\circ}\mathrm{C}$, the scaffold porosity varies with T very slowly; while after $T > 45\,^{\circ}\mathrm{C}$, it varies with T very much faster. To improve the consistency in tissue scaffolds, the dispensing process is suggested to be carried out at temperatures less than a certain value ($45^{\circ}\mathrm{C}$ in this study) in order to minimize the fluctuation of scaffold porosity. Meanwhile, the selection of dispenser temperature should also consider the cell response to the operation conditions such that the biomedical agents (e.g. living cells, growth factors) are able to be incorporated into the fabrication process.

5.4.3 Effect of the Needle Diameter

It is known that the diameter of the dispenser needle can change the flow rate of fluid biomaterial dispensed, thus affect the profile of strand cross-sections. The effect of the needle diameter was investigated with different values of D_n and the simulation results are shown in Figure 5.5.

It can be seen that the size of strand cross-sections increases with an increasing needle diameter. It is not surprising because with the increase of needle diameter, both the friction resistance to flow and the effect of the fluid surface tension decrease, resulting in more fluid biomaterials extruded out of the needle, then larger size of strand cross-sections expected. This relationship is not linear, depending on the fluid surface tension and the flow behaviour of scaffold biomaterials.

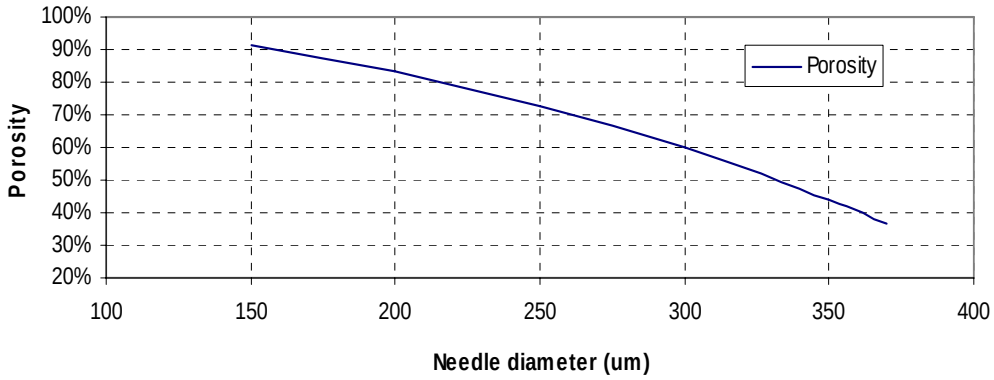

(a). Porosity *vs.* needle diameter

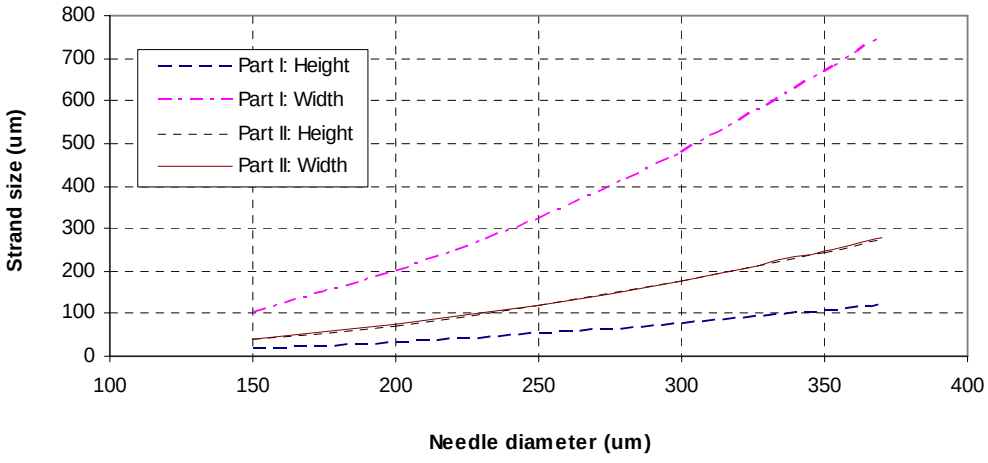

(b). Strand size *vs.* needle diameter

Figure 5.5 Effect of needle diameter, D_n

5.5 Summary

This chapter presented the development of models for the profile of strand cross-sections and the scaffold porosity in the fabrication process. The influence of the air driving pressure, the operation temperature, and the needle diameter, on the fabrication process was investigated by simulations.

The profile of the strand cross-sections is governed by Young-Laplace equation. Combined with the corresponding boundary conditions established, the strand profile and size at different layers and portions can be determined numerically. Based on the geometries of strand cross-sections and the flow rate of dispensed biomaterials, the volume of strands and of the whole tissue scaffold were calculated respectively, thus the scaffold porosity derived.

Simulation results showed that the profile of strand cross-sections and the scaffold porosity can be significantly affected by the air driving pressure, the operation temperature, and the needle diameter. Specifically, for a given moving speed of the dispenser head, the higher driving pressure, the less viscous biomaterial, and the lager needle diameter can result in lager size of the strand cross-section and lower scaffold porosity. The change is nonlinear with the variation of these parameters. The change pattern is affected by the fluid surface tension and the flow behaviour of scaffold biomaterials.

CHAPTER 6

INFLUENCE OF FLUID PROPERTIES ON THE DISPENSING-BASED FABRICATION PROCESS

6.1 Introduction

The dispensing-based fabrication process for tissue scaffolds is usually evaluated by the flow rate of the fluid dispensed, the profile of the strand cross-sections, and the scaffold porosity. Models developed in Chapter 4 and 5 can be used to predict the dispensing-based fabrication process. The accuracy depends much on the characterized fluid properties of scaffold biomaterials such as fluid parameters of non-Newtonian flow behaviour (i.e., the yield stress, τ_y, the consistency index K, and the power law index, n), the fluid surface tension, and the static contact angle, etc. Traditionally the fluid properties for a given material are characterized by using specific instruments, e.g. the rheometer used in Chapter 3. Due to the high sensitivity to temperature, massive measurements are always required in this method and the procedure is usually time-consuming. Moreover, the fluid parameters identified in this way may not be appropriate for predicting the dispensing-based fabrication process, because a little difference between temperatures of the rheometer and the dispensing system may result in a large error in the model prediction, as in the case presented in Chapter 4

For a dispensing-based fabrication process, if the fluid properties were characterized on site, namely, directly from the dispensing system, instead from a rheometer, the influence of the temperature difference can be avoided, thus a more accurate prediction can be achieved. Chapter 4 has shown the effectiveness of such a method for predicting the flow rate of fluid dispensed. In this chapter, it will be extended to be applied in the prediction of the profile and size of strand cross-sections.

The idea behind this method is that the fluid properties, such as non-Newtonian flow behaviour, fluid surface tension, and static contact angle, could be readily identified from a few measurements of the dispensing result. Specifically, the model for the scaffold fabrication process presented previously is considered as a nonlinear function to map the process result for the fabrication performance. Based on the operation parameters and measured data of the flow rate, size of strand cross-sections, the coefficients of the nonlinear function can be estimated by using non-linear least-squares data fitting. In MatLab this process is implemented by the function of:

Beta = nlinfit (**In**, **Out**, 'Model', **Beta0**)

where **Out** is the measured process result, i.e., the flow rate and the size of strand cross-sections; **In** is the known operation conditions, i.e., the applied air pressure, temperature, etc; 'Model' is the model or the nonlinear function for the scaffold fabrication process; **Beta** is the vector of the coefficients associated with the fluid properties. This function starts with the initial coefficient values given by **Beta0,** and then adjusts the coefficient values until the error or the difference between the measured process result and the model prediction is minimal.

6.2 Identify the Fluid Properties from Dispensing Results

To validate the aforementioned method, two sets of dispensing experiment were conducted. One is to identify fluid parameters associated with the non-Newtonian flow behaviour, i.e., K, n, τ_y. The other one is to determine the fluid surface tension and the static contact angle. In this experiment, the fluid Hysol FP® 4451 (provided by Dexter Corporation, USA) was selected for dispensing; and the operation conditions are listed in Table 6.1 except what are specified else.

Table 6.1 Dispensing conditions in experiments

Parameters	**Values**
Air driving pressure	P_g=2.45×10^5 Pa
Temperature	T=45 °C
Moving speed of dispenser needle	V_n=3 mm/s
Distance between needle and substrate	1.5 mm
Needle length	L_n=18 mm
Needle diameter	D_n=920 μm

6.2.1 Identify the non-Newtonian Fluid Parameters

The model to represent the flow rate of fluid dispensed has been presented previously and given here again.

$$Q = \pi(\frac{D_n}{2})^3 n(\frac{\tau_w}{K})^{1/n}(1-\tau_y/\tau_w)^{\frac{n+1}{n}} \cdot [\frac{(1-\tau_y/\tau_w)^2}{3n+1} + \frac{2(\tau_y/\tau_w)(1-\tau_y/\tau_w)}{2n+1} + \frac{(\tau_y/\tau_w)^2}{n+1}] \quad (6.1)$$

Recall Eq. (3.6) of $K = K_0 e^{-T/\lambda}$, for given operation conditions, the above equation can be generally rewritten as the following nonlinear function with three coefficients of K_0, λ, n,

$$Q = Q(K_0, \lambda, n) \quad (6.2)$$

To identify the coefficient values, the dispensing system was controlled to dispense fluid for a time period of 100 seconds with different air driving pressures and temperatures respectively. The measured flow rates, along with the air driving pressures and temperatures, are listed in Table 6.2. Based on the model of Eq. (6.1), the coefficients, K_0, λ, n, were evaluated numerically by least-squares data fitting in MatLab. Their values are given as n=0.6402, K_0=15.61 Pa.s^n, and λ=109.84^{o}C, respectively.

Table 6.2 Measured flow rates at different operation conditions

Experiment	1	2	3	4	5	6	7	8
Air pressure ($\times 10^5$ Pa)	0.98	1.96	2.94	3.92	2.45	2.45	2.45	2.45
Needle temperature (^{o}C)	45	45	45	45	35	45	55	70
Measure flow rate (mg/s)	2.65	8.24	15.34	23.18	4.73	12.27	27.54	51.25

To compare the difference between fluid parameters identified from dispensing result and the ones from the rheometer, this fluid is also characterized by using the rheometer that is described in Chapter 3 (Model: DV-III Rheometer, Brookfield Engineering Lab., USA). A set of flow curves of shear stress *vs.* shear rate was measured at different temperatures, as shown in Figure 6.1. The fluid viscosities were determined from the measurements and the results were shown in Figure 6.2.

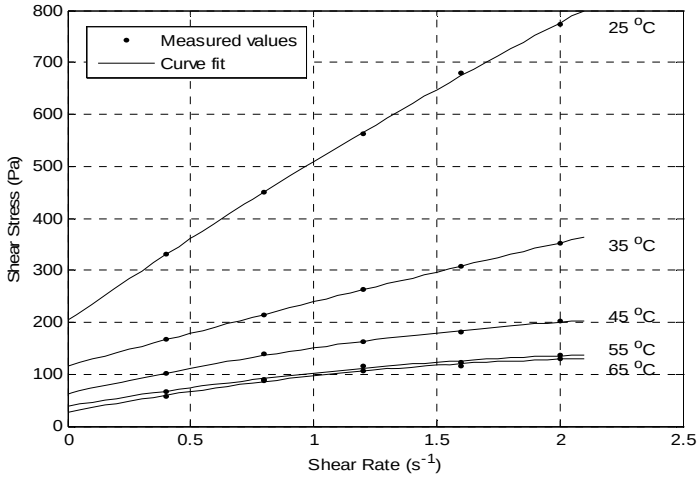

Figure 6.1 Flow curves identified by rheometer

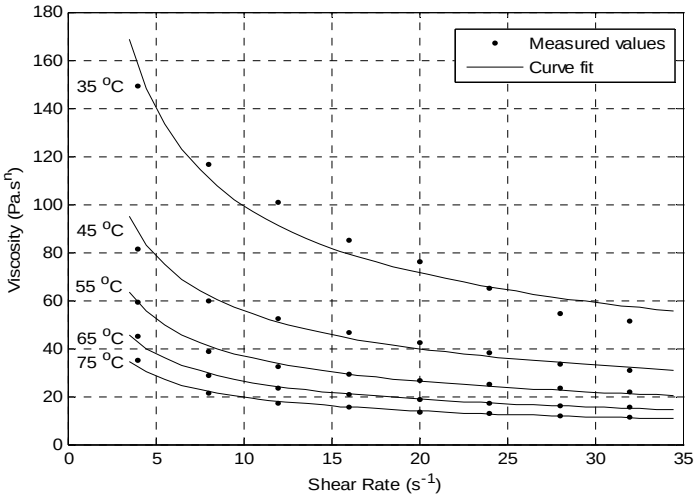

Figure 6.2 Viscosity *vs.* shear rate at different temperatures

It is seen that the viscosity decreases with an increasing shear rate. The curve-fitting parameters were given by n=0.5672, K_0=11.78 Pa.s^n and λ=107.8^{o}C. For comparison, the coefficient values identified from both rheometer and the dispensing experiment are listed in Table 6.3, in which the discrepancy is derived from the temperature difference between the dispensing system and the rheometer.

Table 6.3 Non-Newtonian fluid parameters of Hysol FP® 4451

Flow behaviour related parameters	n	K_0 (Pa.s^n)	λ (^{o}C)
Identified from Rheometer	0.5672	11.78	107.80
Identified from Dispensing experiment	0.6402	15.61	109.84

6.2.2 Identify the Fluid Surface Tension and Contact Angle

Recall the model to represent the profile of strand cross-sections presented in the preceding chapter.

$$\frac{P_{h=0} - \rho g h(x) - P_0}{\sigma} = \frac{h''}{(1+h'^2)^{3/2}} \tag{6.3}$$

The boundary conditions include:

(1) Symmetric shape of the cross-section: $h'(x=0) = \left.\frac{dh(x)}{dx}\right|_{x=0} = 0$.

(2) Static contact angle condition: $h'(x=\frac{W}{2}) = \left.\frac{dh(x)}{dx}\right|_{x=W/2} = -\tan(\theta)$.

(3) Incompressible fluid: $Q = V_n \cdot \int_{-W/2}^{W/2} h(x)dx$.

For given operation conditions, the model of Eq. (6.3) is equivalent to a nonlinear function with the coefficients of the fluid surface tension, σ, and the contact angle, θ, i.e.,

$$h = h(\sigma, \theta) \tag{6.4}$$

To evaluate the values of these two coefficients, the dispensing system was controlled to dispense straight lines on substrates with different temperatures of 45°C - 125°C respectively. Once a fluid line spreads to its equilibrium status, the size of cross-section was measured at five different portions by using a non-contact microscope equipped with an optical measurement system, whose resolution is 1 μm. The experimental data of average width and height of cross-sections were listed in Table 6.4, along with the cross-sectional areas and the substrate temperatures.

Table 6.4 Measurement of size and area of cross-sections at different temperatures

Measurements	Line 1	Line 2	Line 3	Line 4	Line 5
Substrate Temperature (°C)	45	65	85	105	125
Area (mm^2)	3.317	3.389	3.876	4.411	5.089
Width (mm)	3.130	3.583	4.287	4.905	5.566
Height (mm)	1.372	1.357	1.300	1.271	1.296

At each temperature, using the model of Eq. (6.3) and experimental data of width, height and area of cross-sections, the surface tension and contact angle were determined numerically by least-squares data fitting in MatLab. The results are shown in Figure 6.3 and 6.4, respectively.

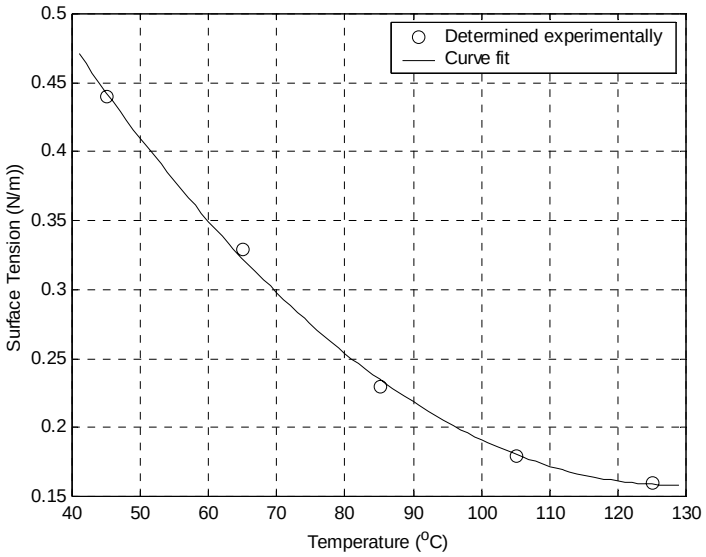

Figure 6.3 Surface tension *vs.* temperature

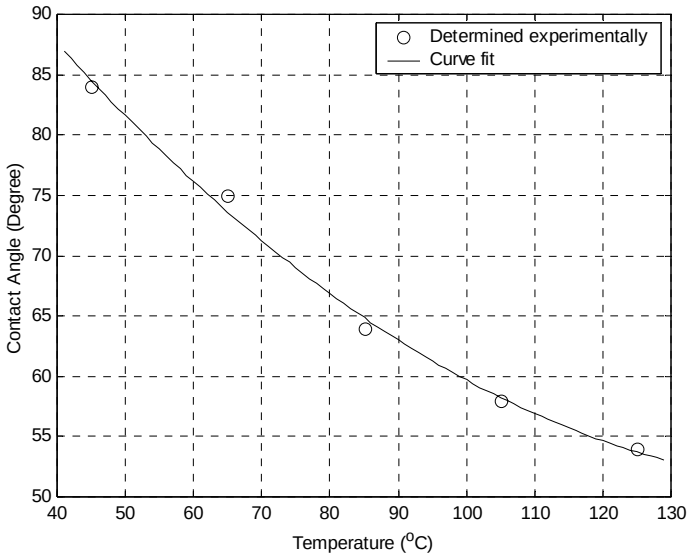

Figure 6.4 Contact angle *vs.* temperature

6.3 Verify the Predictions of Dispensing-based Fabrication Process

The fluid properties, i.e. the non-Newtonian flow behaviour, the surface tension, and the contact angle, have been identified from the dispensing experiments. The values could be used to predict the dispensing-based fabrication process. To illustrate the effectiveness of such identified fluid properties, dispensing experiments were conducted again by using a different set of operation conditions and then the results were compared with model predictions.

6.3.1 Verify the Predicted Flow Rates of Fluid Dispensed

Dispensing-based fabrication process was carried out at the driving pressure of P_g = 2.45×10^5 Pa with different temperatures, and at the temperature of T = 45 ^{o}C with different driving pressures, respectively. As in the previous experiments, the average flow rate was measured again and the results are given in Figure 6.5 for different temperatures and Figure 6.6 for different driving pressures.

Based on model of Eq. (6.1), simulations were performed to predict the flow rate of dispensed fluid at different operation conditions. The result is also shown in Figure 6.5 and 6.6 for comparison. The solid line with a legend of *Model Prediction I* presents the flow rate predicted based on the flow behavior identified from previous dispensing experiments. The dash line with a legend of *Model Prediction II* represents that the flow rate predicted based on the flow behavior identified from a rheometer.

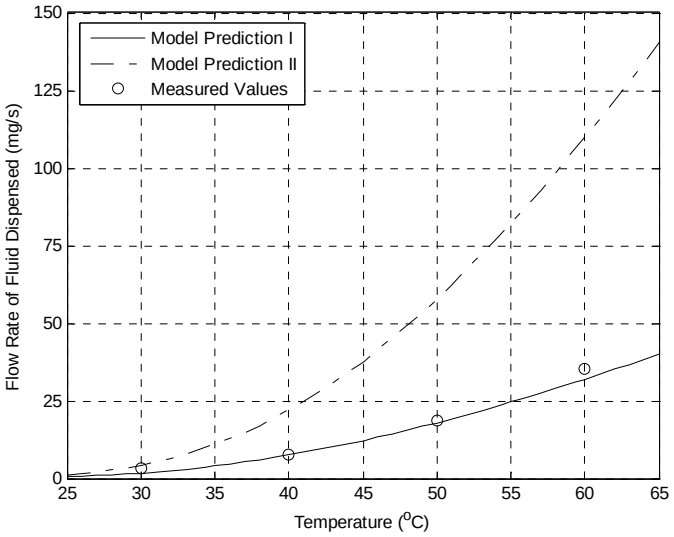

Figure 6.5 Flow rate *vs.* needle temperature at $P_g = 2.45 \times 10^5$ Pa.

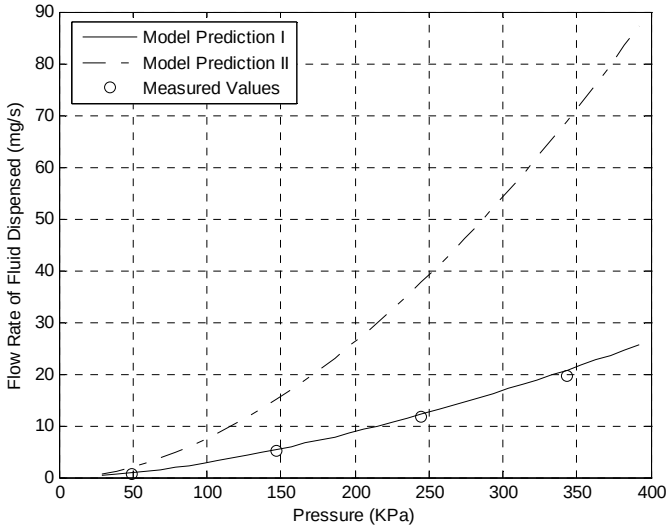

Figure 6.6 Flow rate *vs.* air driving pressure at $T = 45\ ^{o}$C.

It can be seen that *Model Prediction I* has a closer agreement with the measured values, indicating that the flow behaviour identified from the dispensing experiments are effective for

the flow rate prediction. The *Model Prediction II* has a relatively large error, which is mainly caused by the temperature difference between the dispensing system and the rheometer.

6.3.2 Verify the Predicted Profile of Cross-sections

In this experiment, two sets of fluid lines were dispensed. One was on the substrate with different temperatures under the same driving pressure of P_g = 2.45×10^5 Pa; and the other one was dispensed on the substrate of T = 100 ^{o}C by applying different driving pressures. As in the previous experiments, the size and area of line cross-sections were measured and the results were given in Table 6.5 for the case of different temperatures. For the other set of lines, the measured widths and heights are shown in Figure 6.7 and 6.8 with corresponding cross-sectional areas.

Based on the model of Eq. (6.3), simulations were performed to predict the profile of line cross-sections by using the values of surface tension and contact angle identified from previous dispensing experiments. The simulation results for the case of different temperatures are also listed in Table 6.5. Predictions for the other set of lines are shown as solid lines in Figure 6.7 and 6.8.

Table 6.5 Profile of the strand cross-section at different temperatures

	Line 1	Line 2	Line 3	Line 4	Line 5
Board Temperature (^{o}C)	45	65	85	105	125
Area (mm^2)	6.914	7.146	8.638	9.762	11.206
Predicted width (mm)	4.56	5.30	6.42	7.53	8.63
Measured width (mm)	4.52	5.15	6.40	7.39	8.50
Predicted height (mm)	1.98	1.84	1.84	1.79	1.78
Measured height (mm)	2.01	1.83	1.83	1.78	1.79

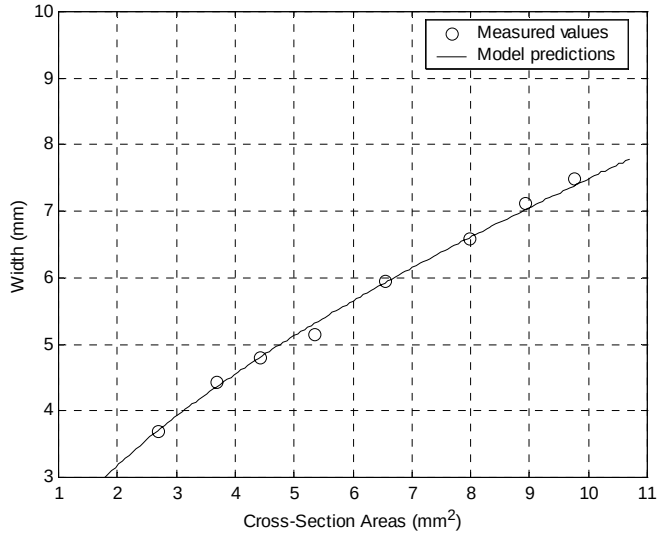

Figure 6.7 Measured and predicted widths of the strand cross-section at T = 100 ^{o}C.

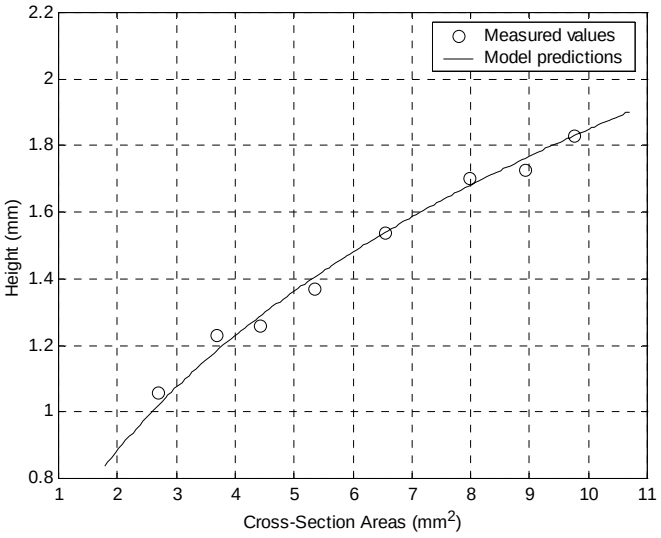

Figure 6.8 Measured and predicted heights of the strand cross-section at T = 100 ^{o}C.

It can be seen that for both cases, the predicted widths and heights agree well with the measured ones. This indicates that the fluid surface tension and contact angle identified from the dispensing experiments are effective to be used for predicting the profile of strand cross-sections, thereby making it possible to specify their influence on the dispensing-based fabrication process.

6.4 Summary

In this chapter, a method was presented to characterize the fluid properties from a few dispensing measurements, instead of from a rheometer. Experimental results showed that the fluid properties thus identified are very promising to predict the dispensing-based fabrication process. In these experiments, the material Hysol FP® 4451 was used for dispensing. However this method can be readily extended and applied to other scaffold biomaterials used in tissue engineering. Also, it provides a cost- and time-efficient way to characterize the fluid properties from the dispensing experiments. For some other applications, it should be aware that the flow behaviour of Hysol FP® 4451 obtained in this study may not be as effective as what has been illustrated in this chapter because of the possible temperature difference between the present dispensing system and the system to which the material is to be applied.

CHAPTER 7
CONCLUSIONS AND FUTURE WORK

7.1 Conclusions

Dispensing-based RP techniques have been widely used in the tissue scaffold fabrication, which is an interdisciplinary area involving precise fluid manipulation, material science, advanced manufacturing, and biomedical technologies, etc. The research presented in this thesis carried out a comprehensive study on the dispensing-based fabrication process, with the objective of identifying the influence of various parameters on the fabrication performance. The main contributions from this study are summarized as follows.

(1) To characterize scaffold materials in terms of biocompatibility, a comparative study was carried out to evaluate DRG neuron response *in vitro* to different biomaterials including PLLA, PCL, collagen, chitosan, and gelatine. Cell adhesion and neurite outgrowth were monitored and analyzed statistically on thin films that were individually made from the examined biomaterials. The experimental results showed that chitosan is a very promising biomaterial for nerve tissue scaffolds as applied to the PNS nerve repair and regeneration applications.

(2) A model to represent the flow rate of fluid biomaterials dispensed in the scaffold fabrication process was developed, in which the influence of fluid surface tension is taken into account. To validate the developed model, experiments were carried out on a commercial automated fluid dispensing system (C-720, Asymtek, USA). The experimental results was compared to the model predictions, in which the flow behaviour was identified from a few dispensing measurements and a rheometer, respectively. It is shown that the model predictions based on the flow behaviour identified from the dispensing measurements are in good agreement with the experimental results, while the model predictions based on the flow behaviour identified from a rheometer have a relatively large error, which is derived from the temperature difference between the dispensing system and the rheometer.

(3) The profile of strand cross-sections was modeled based on the Young-Laplace equation. Combined with the established boundary conditions, the size and profile of the strands could be determined at different layers and portions. The scaffold porosity for measuring the interconnected pore space was evaluated as well. Simulation results showed that the developed model can be used to investigate the effects of air driving pressure, temperature, and needle diameter, on the fabrication process, with the following observations:

For a given moving speed of the dispenser needle, a higher driving pressure, a higher temperature, and a larger needle diameter result in a higher flow rate but a lower porosity. The variation is nonlinear, and is affected by the non-Newtonian flow behaviour and the fluid surface tension of scaffold materials.

The size of strand cross-sections increases with an increasing temperature, in which the change of width at Part I, W_I, is the most sensitive. When the temperature of the dispenser head is less than a certain value (45 ^oC in this study), the scaffold porosity varies slowly with temperature; while after that value the variation becomes much faster.

(4) A method was developed to characterize the fluid properties, including the flow behaviour, the surface tension, and the contact angle, from a few dispensing measurements, instead by using specific instrument. With this method, the influence of the temperature difference between the fabrication system and the identification instrument can be avoided, thus a more accurate prediction is expected. Experimental results showed the effectiveness of such an identification method for the predictions of the dispensing-based fabrication process.

7.2 Future work

There are a number of issues that arise from the present study and need to be further addressed. For this purpose, the following recommendations are suggested for the future work.

1. Characterization of the material biocompatibility *in vivo.*

For tissue scaffold materials, besides the *in vitro* biocompatibility studied in this research, their *in vivo* biocompatibility, like the implant degradation and new tissue regeneration, is also required for the material characterization. Furthermore, the material biocompatibility could be improved by surface coating process, or incorporation of other additives or fillers. More research needs to be conducted.

2. Investigation into the relationship between the microstructure of scaffolds and their mechanical properties, i.e., the structure-function relationship.

For a given application to design a tissue scaffold, there could be much many solutions for the scaffold microstructure. Understanding the relationship between the mechanical properties (e.g. effective elastic modulus, resistant strength) and the microstructures (e.g. pore size, spatial distribution, and porosity) is essential to achieve the optimal design in such a project. For this purpose, the representative volume element and finite element method could be an effective method to be used.

3. Experimental verification for the models of strand profile and scaffold porosity.

The model to represent the strand profile and the scaffold porosity has been developed in this research. The experimental verification, however, is still lack due to the time and instrument limitations. For the experiments, the tissue scaffold could be designed with different micro-structures and numerous layers to mimic a real tissue composition. The scaffold biomaterial is dispensed in a controlled manner under various operation conditions. Once fabrication process completed, the size of the strand cross-sections at different layers and portions can be measured based on the scanning electron microscopy (SEM) analysis. A mercury porosimeter can be used to determine the scaffold porosity. The effectiveness of models is determined based on the comparison between the measured data and the simulation results.

REFERENCES

[1] Adamson, A.W. and Gast, A.P., 1997, *Physical Chemistry of Surfaces*, John Wiley & Sons, New York.

[2] Anderson, J., 1998, "Biocompatibility of Tissue Engineered Implants," In: Patrick, *Frontiers in Tissue Engineering*, Pergamon, pp. 152-165.

[3] Ang, T.H. and Sultana, F.S.A., 2002, "Fabrication of 3-D Chitosan-hydroxyapatite Scaffolds using a Robotic Dispensing System," *Material Science Eng*, vol. 20, pp. 35- 42.

[4] Barnes, H.A., Hutton, J.F., and Walters, K., 1989, *An Introduction to Rheology*, Elsevier Science Publishers B. V., pp. 1-37.

[5] Bensaïd, W. and Triffitt, J. T., 2003, "A Biodegradable Fibrin Scaffold for Mesenchymal Stem Cell Transplantation," *Biomaterials*, vol. 24(14), pp. 2497-2502.

[6] Bogue, D.C., 1959, "Entrance Effects and Prediction of Turbulence in non-Newtonian Flow," *Ind. Eng. Chem.*, vol. 51, pp. 874.

[7] Boyan, B.D. and Hummert, T.W., 1996, "Role of Material Surfaces in Regulating Bone and Cartilage Cell Response," *Biomaterials*, vol. 17(2), pp. 137–46.

[8] Bredt, J.F., Sach, E., Brancazio, D., Cima, M., Curodeau, A., and Fan, T., 1998, *Three dimensional printing system*, US Patent 5807437.

[9] Brockes, J. P., Fields, K.L., and Raff, M.C., 1979, "Studies on Cultured Rat Schwann Cells. I. Establishment of Purified Populations from Cultures of Peripheral Nerves," *Brain Research*, vol. 165, pp. 105-118.

[10] Chen, C.S., Mrksich, M., Huang, S., and Whitesides, G.M., 1997, "Geometric Control of Cell Life and Death," *Science*, vol. 276, pp. 1425–28.

[11] Chen, X.B. and H. Ke, 2006, "Effects of Fluid Properties on Dispensing Processes for Electronics Packaging," *IEEE Trans. On Electronics Packaging Manufact,* vol. 29, no. 2, pp. 75-82.

[12] Chen, X.B., 2006, "Modeling of Rotary Screw Fluid Dispensing Process," *ASME Journal of Electronic Packaging* (in press)

[13] Chen, X.B., and J. Kai, 2004, "Modelling of Positive-Displacement Fluid Dispensing Processes," *IEEE Trans. On Electronics Packaging Manufact.*, vol. 27, no. 3, pp. 157-163

[14] Chen, X.B., Schoenau, G., and Zhang, W.J., 2000, "Modeling of Time-pressure Fluid Dispensing Process," *IEEE Trans. on Electronics Packaging Manu.*, vol. 23, pp. 300–305.

[15] Chhabra, R.P. and Richardson, J.F., 1999, *Non-Newtonian Flow in the Process Industries*, Butterworth-Heinemann.

[16] Chua, C.K. and Leong, K.F., 1997, *Rapid prototyping: principles of applications and manufacturing*, John Wiley & Sons, Singapore.

[17] Fang, Z., Starly, B., and Sun, W., 2005, "Computer-aided Characterization for the Effective Mechanical Properties of Porous Tissue Scaffolds," *Computer-Aided Design*, vol. 37, pp. 65-72.

[18] Finke, S. and Feenstra, F.K., 2002, "Solid freeform fabrication by extrusion and deposition of semi-solid alloys," *Journal of Materials Science*, vol. 37(15), pp. 3101-3106.

[19] Flynn, L., Dalton, P.D., and Shoichet, M.S., 2003, "Fibre Templating of Poly (2-hydroxyethyl methacrylate) for Neural Tissue Engineering," *Biomaterials*, vol. 24(23), pp. 4265-72.

[20] Foust, A.S., 1960, *Principles of Unit Operations*, John Wiley & Sons, New York, pp. 542.

[21] Freed, L.E., Vunjak-Novakovic, G., and Biron, R.J., 1994, "Biodegradable polymer

scaffolds for tissue engineering," *Biotechnology*, vol. 12, pp. 689–93.

[22] Fry, E.J., 2001, "Central Nervous System Regeneration: Mission Impossible," *Clin Exp Pharmacol Physiol*, vol. 28, pp. 253-258.

[23] Gerburg, K. and Felix, S., 2003, "Bio-compatibility of type I/III Collagen Matrix for Peripheral Nerve Reconstruction," *Biomaterials*, vol. 24, pp. 2778-87.

[24] Grande, D.A. and Halberstadt, C., 1997, "Evaluation of Matrix Scaffolds for Tissue Engineering of Articular Cartilage Grafts," *J Biomedical Mater Res*, vol. 34, pp. 211–20.

[25] Han, S. and Wang, K. K., 1997, "Analysis of the Flow of Encapsulant during Underfill Encapsulation of Flip-Chips," *IEEE Trans on Components, Packaging, and Manu Tech.-Part B*, vol. 20, pp. 424-433.

[26] Hayashi, T., 1994, "Biodegradable Polymers for Biomedical Uses," *Prog Polym Sci*, vol. 19, pp. 663-702.

[27] Heath, C.A. and Rutkowski, G.E., 1998, "The Development of Bioartificial Nerve Grafts for Peripheral Nerve Regeneration," *Trends Biotech*, vol. 16, pp. 163-168.

[28] Hutmacher, D.W., 2000, "Polymeric Scaffolds in Tissue Engineering Bone and Cartilage," *Biomaterials*, vol. 21, pp. 2529–2543.

[29] Hutmacher, D.W., 2001, "Scaffold Design and Fabrication Technologies for Engineering Tissues-state of the Art and Future Perspectives," *J Biomaterial Science-Polymer E*, vol. 12, pp. 107-124.

[30] Kim, S.E. and Park, J.H., 2003, "Porous Chitosan Scaffold Containing Microspheres Loaded with Transforming Growth Factor-β_1: Implications for Cartilage Tissue Engineering," *J. Controlled Release*, vol. 91, pp. 365–374.

[31] Kim, S.S. and Utsunomiya, H., 1998, "Survival and Function of Hepatocytes on a Novel

Three-dimensional Synthetic Biodegradable Polymer Scaffold with an Intrinsic Network of Channels," *Ann Surgery*, vol. 228(1), pp. 8–13.

[32] Kruth, J.P., 1991, "Material Increase Manufacturing by Rapid Prototyping Techniques," *Ann CIRP*, vol. 40(2), pp. 603–14.

[33] Landers, R. and Mulhaupt, R., 2000, "Desktop Manufacturing of Complex Objects, Prototypes and Biomedical Scaffolds by means of Computer-assisted Design Combined with Computer-guided 3-D Plotting of Polymers and Reactive Oligomers," *Macromol Mater Eng.*, vol. 282, pp. 17-21.

[34] Landers, R., 2002, "Rapid Prototyping of Scaffolds Derived from Thermoreversible Hydrogels and Tailored for Applications in Tissue Engineering," *Biomaterials*, vol. 23, pp. 4437–4447.

[35] Langer, R. and Vacanti, J.P., 1993, "Tissue Engineering," *Science*, vol. 260, pp. 920-926.

[36] Lee, J.E., and Kim, K.E., 2004, "Effects of the Controlled-released TGF-β_1 from Chitosan Microspheres on Chondrocytes Cultured in a Collagen / Chitosan / Glycosaminoglycan Scaffold," *Biomaterials*, vol. 25, pp. 4163–4173.

[37] Lindsay, R.M., 1988, "Nerve Growth Factors (NGF, BDNF) Enhance Axonal Regeneration but are not Required for Survival of Adult Sensory Neurons," *Journal of Neuroscience*, vol. 8, pp. 2394-2405.

[38] Matsumoto, H. and Fujikawa, K., 2001, "Leeds-Keio Artificial Ligament: A New Concept for the Anterior Cruciate Ligament Reconstruction of the Knee," *Keio Journal of Medicine*, vol. 50 (3), pp. 161-166.

[39] McClary, K.B., Ugarova, T., and Grainger, D.W., 2000, "Modulating Fibroblast Adhesion, Spreading and Proliferation using Self-assembled Monolayer Films of Alkylthiolates on

Gold," *J Biomedical Mater Res*, vol. 50(3), pp. 429–39.

[40] Middleton, J.C. and Tipton, A.J., 2000, "Synthetic Biodegradable Polymers as Orthopedic Devices," *Biomaterials*, vol. 21, pp. 2335-2346.

[41] Mikos, A.G., Sarakinos, G., Vacanti, J.P., Langer, R., and Cima, L.G., 1996, *Biocompatible polymer membranes and methods of preparation of three dimensional membrane structures*, US Patent Number 5514378.

[42] Mooney, D.J., Cima, L.G., and Langer, R., 1992, "Principles of Tissue Engineering and Reconstruction using Polymer-cell Constructs," *Mater Res Soc Symp Proc*, vol. 52, pp. 45.

[43] Nehrer, S., Breinan, H.A., and Ramappa, A., 1997, "Canine Chondrocytes Seeded in type I and type II Collagen Implants Investigated *in vitro*," *J Biomedical Mater Res*, vol. 38, pp. 95-104.

[44] Onishi, H. and Machida, Y., 1999, "Biodegradation and Distribution of Water-soluble Chitosan in Mice," *Biomaterials*, vol. 20, pp. 175–182.

[45] Palsson, B. and Bhatia, S.N., 2004, *Tissue Engineering*, Pearson Prentice Hall, New Jersey, pp. 261-269.

[46] Panton, R. L., 1996, *Incompressible Flow*, John Wiley and Sons, New York.

[47] Pesakova, V., Stol, M., and Adam, M., 1990, "Comparison of the Influence of Gelatine and Collagen Substrates on Growth of Chondrocytes," *Folia Biol (Praha)*, vol. 36, pp. 264–270.

[48] Philbrook, K.F., Sanders, J.R., Royden, C., and Forsyth, J.L., 1996, *3-D model maker*, US Patent 5506607.

[49] Pieper, J.S., Kraan, P.M., and Hafmans, T., 2002, "Crosslinked type II Collagen Matrices: Preparation, Characterization, and Potential for Cartilage Engineering," *Biomaterials*, vol. 23, pp. 3183-3192.

[50] Ponticiello, M.S. and Schinagl, R.M., 2000, "Gelatin-based Resorbable Sponge as a Carrier Matrix for Human Mesenchymal Stem Cells in Cartilage Regeneration Therapy," *J Biomedical Mater Res*, vol. 52, pp. 246-255.

[51] Robinson, B., Hollinger, J.O., Szachowicz, E., and Brekke, J., 1995, "Calvarial Bone Repair with Porous dl-polylactide," *Otolaryng Head Neck*, vol. 112(6), pp. 707–13.

[52] Schmidt, C.E. and Leach, J.B., 2003, "Neural Tissue Engineering: Strategies for Repair and Regeneration," *Annual Review of Biomedical Engineering*, Vol. 5, pp. 293-347.

[53] Schreyer, D.J. and Skene, J.H.P, 1991, "Fate of GAP-43 in Ascending Spinal Axons of DRG Neurons after Peripheral Nerve Injury: Delayed Accumulation and Correlation with Regenerative Potential," *Journal of Neuroscience*, vol. 11, pp. 3738-3751.

[54] Schwab, M.E., 1998, "Regenerative Nerve Fibre Growth in the Adult Central Nervous System," *News Physiol Sci*, vol. 13, pp. 294-298.

[55] Scott, C.S., 1991, *Apparatus and method for creating three-dimensional objects*, US Patent 5121329.

[56] Shalak, R. and Fox, C.F., 1988, *Tissue Engineering*, Alan R. Liss, New York, pp. 26-29.

[57] Skelland, A.H.P., 1967, *Non-Newtonian Flow and Heat Transfer*, John Wiley & Sons, New York, pp. 1-14.

[58] Suh, J.K., 2000, "Application of Chitosan-based Polysaccharide Biomaterials in Cartilage Tissue Engineering: a Review," *Biomaterials*, vol. 21, pp. 2589-98.

[59] Sundback, C.A. and Shyu, J.Y., 2005, "Biocompatibility Analysis of Poly (glycerol sebacate) as a Nerve Guide Material," *Biomaterials*, vol. 26, pp. 5454–5464.

[60] Thompson, R.C., Yaszemski, M.J., Powers, J.M., and Mikos, A.G., 1995(a), "Fabrication of Biodegradable Polymer Scaffolds to Engineering Trabecular Bone," *J Biomaterial Science-*

Polymer E, vol. **7**, pp. 23-38

[61] Too, M.H. and Leong, K.F., 2002, "Investigation of 3D Non-Random Porous Structures by Fused Deposition Modelling," *International Journal of Advanced Manufacturing Technology*, vol. 19, pp. 217-223.

[62] Vanderploeg, E. J. and Imler, S.M., 2004, "Oscillatory Tension Differentially Modulates Matrix Metabolism and Cytoskeletal Organization in Chondrocytes and Fibrochondrocytes," *Journal of Biomechanics*, vol. 37(12), pp. 1941-1952.

[63] Vert, M., Li, M.S., Spenlehauer, G., and Guerin, P., 1992, "Bioresorbability and Biocompatibility of Aliphatic Polyesters," *J Material Science*, vol.3, pp. 432-46.

[64] Vozzi, G. and Previti, A., 2002, "Microsyringe-based Deposition of 2D and 3D Polymer Scaffolds with a Well-defined Geometry or Application to Tissue Engineering," *Tissue Engineering*, Vol. 8(6), pp. 1089-98.

[65] Wakitani, S. and Goto, T., 1994, "Mesenchymal Cell-Based Repair of Large, Full-Thickness Defects of Articular Cartilage," *Journal of Bone & Joint Surgery*, vol. 76-A (4), pp. 579-592.

[66] Weiss, L.E. and Amon, C.H., 2005, "Bayesian Computer-aided Experimental Design of Heterogeneous Scaffolds for Tissue Engineering," *Computer-Aided Design*, vol. 37(11), pp. 1127-1139.

[67] Whang, K., Thomas, C.K., Nuber, G., and Healy, K.E., 1995, "A Novel Method to Fabricate Bioabsorbable Scaffolds," *Polymer*, vol. 36, pp. 837.

[68] White, F. M., 2003, *Fluid Mechanics (the 5th edition)*, McGraw-Hill, New York.

[69] Widmer, M.S. and Mikos, A.G., 1998, "Fabrication of Biodegradable Polymer Scaffolds for Tissue Engineering," in *Frontiers in tissue engineering*, Patrick, C.W., Mikos, A.G., Elsevier Science, New York, pp. 107-20.

[70] Wilkinson, W.L., *Non-Newtonian Fluids*, New York: Pergamon, 1960.

[71] Woodfield, T.B.F. and Malda, J., 2004, "Design of Porous Scaffolds for Cartilage Tissue Engineering using a Three-dimensional Fibre-deposition Technique," *Biomaterials*, vol. 25 (18), pp. 4149-4161.

[72] Yannas, I.V., Lee, E., and Orgill, D.P., 1989, "Synthesis and Characterization of a Model Extracellular Matrix that Induces Partial Regeneration of Adult Mammalian Skin," *Proc Natl Acad Science*, vol. 86, pp. 933.

[73] Yu, T.T. and Shoichet, M.S., 2004, "Guided Cell Adhesion and Outgrowth in Peptide-modified Channels for Neural Tissue Engineering," *Biomaterials*, vol. 26(13), pp. 1507-14.

[74] Zein, I. and Hutmacher, D.W., 2002, "Fused Deposition Modeling of Novel Scaffold Architectures for Tissue Engineering Applications," *Biomaterials*, vol. 23(4) pp. 1169-85.

[75] Zeltinger, J. and Sheerwood, J.K., 2001, "Effects of Pore Size and Void Fraction on Cellular Adhesion, Proliferation, and Matrix Deposition," *Tissue Engineering*, vol. 7(5), pp. 557-572.

APPENDIX

1. Computer Programs Used in the Present Research

[1]. Program used by the rheometer to identify the flow behaviour of chitosan solution in Chapter 3.

```
WTI    00:30;              % Wait for 30 sec for material initialization
SSN    1.00;               % Set rotation speed (RPM) of Cone
WTI    00:30;              % Rotate for 30 sec
DSP                        % Display the measured data
LSC    6;                  % Set loop number
SSI    2 .00;              % Set rotation speed increment (RPM) at each loop
WTI    00:30;              % At each new rotation speed, rotate for 30 sec
DSP                        % Display the measured data
LEC                        % Loop end
FSO   C:\Documents and Settings\My Documents\chitosan.DB;    % Save data file
```

[2]. Program for Curve-fitting of experimental data of the viscous consistency index (K) in Chapter 3.

```
% Curvefitting_K.m is used to curve-fit the values of K_0 and Lambda for the viscous
  consistency index, K

T_m=[ 26.4  35.3   40.3   45.2   55.3   65.1   75.2 ]';   % Temperature settings on rheometer (oC)
K_m=[ 1023  675.3  571.3  471.7  286.2  276.4  163.2 ]';   % Measured data of K (cP)

x0=[2000 50];    % Initial point of (K_0 Lambda)
[x,resnorm] = lsqcurvefit(@exp_K_fun, x0, T_m, K_m);
K_0=x(1)
Lambda=x(2)

% Compare the curve-fitting parameters to experimental data
T=20:1:80;
```

```
K=K_0.*exp(-T./Lambda);
plot (T_m,K_m,'o', T,K,'-');
legend ('Measured data', 'Curve fitting: K = 2824*exp( - T / 25.42)');
grid;
xlabel ('Temperature (^oC)');
ylabel ('K (cP)');

% the function of exp_K_fun.m is used in Curvefitting_K.m
function F = exp_K_fun(x,T_m)
F = x(1).*exp(-T_m./x(2));          % the viscous consistency index: K=K_0*exp(-T/Lambda)
```

[3]. Program used in Chapter 4 to identify the fluid properties from a few dispensing experiments, and to simulate the flow rate of biomaterials dispensed.

```
% filename: FlowRate_July2006.m
% This program is used to investigate the performance of the flow rate in the scaffold
    fabrication, which include:

% 1. Identify the parameters: n, K0, and Lambda (K = K0*exp (-T/Lambda)
% 2. Verify the model by using the experiments results under the dispensing conditions which
    are different from the parameter identification in (1).
 clc, clear, clf,
global Den Dn Ln Dh Lh Ls Da La;

% 1. Experimental settings
    n =  0.48;              % Fluid flow behaviour index
    Den = 1000.0;       % Fluid density (Kg/m^3)
    C2_st = 4.11e-5;   % Coefficients associated with the surface tension
    C1_st = -0.0105;   % S_tension = C2_st*T3^2 + C1_st*T3 + C0_st
    C0_st = 0.8336;    % where T3 is the needle temperature
    Da = 2.32e-3;       % Adapter internal diameter (m)
    La = 10.0e-3;       % length (m)
    Dh = 2.32e-3;      % Needle heater internal diameter (m)
    Lh = 18.55e-3;     % length (m)
    Dn = 0.2e-3;        % Needle internal diameter (m)
    Ln = 18.0e-3;       % length (m)
```

```
% 2. Estimate of [n K0 TK]
    FR_M = [0.554, 1.203, 3.256, 8.764, 17.162];       % Measured flow rate (mg/s)

    % Dispensing conditions
    V_P  = [0.5, 1.0, 1.5, 2.0, 2.5]*1.0e+5;     % Pressure (Pa)
    V_T1 = [32.8, 25.0, 28.2, 30.8, 32.8];      % Adapter temperature (oC)
    V_T2 = [58.2, 25.0, 35.1, 46.7, 58.2];      % Needle heater temperature (oC)
    V_T3 = [40.4, 25.0, 30.6, 35.8, 40.4];      % Needle temperature (oC)
    V_St = 2*(C2_st*V_T3.^2 + C1_st*V_T3 + C0_st)/6/Dn;    % Fluid surface tension (N/m)
    Input_model =  [FR_M; V_P - V_St; V_T1; V_T2; V_T3];
    Err = [0 0 0 0 0];              % Given relative error
    Paras = [0.6 10 100];       % initial parameter estimates of [n K0 TK]
    parashat = nlinfit (Input_model, Err, 'Relative_error_fun_July2006', Paras);
    clear FR_M   V_P   V_T1   V_T2    V_T3   V_St

    n = parashat(1)               % Parameters identified from the dispensing experiments
    K0 = parashat(2)
    Lambda = parashat(3)
    n_r = 0.89;                   % Parameters identified from the rheometer
    K0_r = 2824/1000;             % unit cP to Pa.s
    Lambda_r = 25.42;



% 3. Model verification
    FR_M = [0.30, 1.203, 2.327, 4.890,   8.498
                0.347, 1.342, 3.256, 6.163,   9.822
                0.476, 1.998, 4.841, 8.764,  13.760
                0.554, 2.847, 6.633, 11.251, 17.132];     % Measured flow rate (mg/s)

    % Dispensing conditions
    V_P  = [0.5, 1.0, 1.5, 2.0, 2.5]*1.0e+5;        % Pressure (Pa)
    V_T1 = [25.0, 28.2, 30.8, 32.8];                % Adapter temperature (oC)
    V_T2 = [25.0, 35.1, 46.7, 58.2];                % Needle heater temperature (oC)
    V_T3 = [25.0, 30.6, 35.8, 40.4];                % Needle temperature (oC)
    V_St = 2*(C2_st*V_T3.^2 + C1_st*V_T3 + C0_st)/6/Dn;      % Fluid surface tension (N/m)
```

```
for i = 1:4              % 4 levels of temperature
   Q_measured = FR_M(i,:);       % Measured flow rate (mg/s)
   Ta = V_T1(i);                 % Adapter temperature (oC)
   Th = V_T2(i);                 % Needle heater temperature (oC)
   Tn = V_T3(i);                 % Needle temperature (oC)
   P_simu = [0.1:0.1:3.0]*1.0e+5 - V_St(i);

% Model prediction based on the parameter values from dispensing experiments
      Ka = K0*exp (-Ta/Lambda);
      md = pi*n*Da^((3*n+1)/n)/(2^(3*n+2)*(3*n+1)*La^(1/n));
      c1  = md/(Ka^(1/n));
      Kh = K0*exp (-Th/Lambda);
      md = pi*n*Dh^((3*n+1)/n)/(2^(3*n+2)*(3*n+1)*Lh^(1/n));
      c2  = md/(Kh^(1/n));
      Kn = K0*exp (-Tn/Lambda);
      md = pi*n*Dn^((3*n+1)/n)/(2^(3*n+2)*(3*n+1)*Ln^(1/n));
      c3  = md/(Kn^(1/n));
  c = 1/(1/c1 + 1/c2 + 1/c3);
  Q_simulated = c*P_simu.^(1/n);              % Simulated flow rate (m^3/s)
  Q_simulated = Q_simulated*Den*1.0e6;    % Simulated flow rate (mg/s)

% Model prediction based on the parameter values from a rheometer
      Ka = K0_r*exp (-Ta/Lambda_r);
      md = pi*n_r*Da^((3*n_r+1)/n_r)/(2^(3*n_r+2)*(3*n_r+1)*La^(1/n_r));
      c1  = md/(Ka^(1/n_r));
      Kh = K0_r*exp (-Th/Lambda_r);
      md = pi*n_r*Dh^((3*n_r+1)/n_r)/(2^(3*n_r+2)*(3*n_r+1)*Lh^(1/n_r));
      c2  = md/(Kh^(1/n_r));
      Kn = K0_r*exp (-Tn/Lambda_r);
      md = pi*n_r*Dn^((3*n_r+1)/n_r)/(2^(3*n_r+2)*(3*n_r+1)*Ln^(1/n_r));
      c3  = md/(Kn^(1/n_r));
  c = 1/(1/c1 + 1/c2 + 1/c3);
  Q_simulated_r = c*P_simu.^(1/n_r);              % Simulated flow rate (m^3/s)
  Q_simulated_r = Q_simulated_r*Den*1.0e6;   % Simulated flow rate (mg/s)
  Plot (P_simu*1.0e-3,Q_simulated_r,'k-.', V_P*1.0e-3,Q_measured, 'ko');
  legend ('Model Prediction','Measured Values',2)
  grid;
```

```
    xlabel ('Applied Pressure (KPa)');
    ylabel ('Flow Rate of the Biomaterial Dispensed (mg/s)');
    pause; clf;
    Plot (P_simu*1.0e-3, Q_simulated_r, 'k-.', P_simu*1.0e-3, Q_simulated, 'k-', V_P*1.0e-3,
          Q_measured, 'ko');
    legend ('Model Prediction I','Model Prediction II', 'Measured Values',2)
    grid;
    xlabel ('Applied Pressure (KPa)');
    ylabel ('Flow Rate of the Biomaterial Dispensed (mg/s)');
    pause; clf;
  end
% The End
```

[4]. Program used in Chapter 5 to simulate the profile of strand cross-sections and scaffold porosity.

```
% FILE NAME: shape.m
% This program is used to calculate the shape of fluid formed on the board from a given volume
   (V0),by combining with the Simulink Model filed shape_model.mdl.
V_n=2.5/1000;          % Moving speed of dispenser needle (m/s)
Q=1.4940e-010;         % volume flow rate (m^3/s)
A0=Q/V_n;              % Area of the lateral scation (m*m)
st=0.073;              % Surface Tension (N/m)
sita=35;               % Static Angle (degree)
g=9.8;                 % Gravity Accelaration(N/Kg)
L_x=800e-6;            % Distance between 2 strands (m)

% (1) Considering the gravity influence
   den=1000;           % Density (Kg/(m*m*m))
   P0=0;
   del_Area=2;         % (mm*mm)
   while del_Area > 0.01*A0*10^6
     P0=P0+0.1;
     [t,x,y]=sim ('shape_model_thesis');
     del_Area=abs (2*y(end,2)-A0)*10^6; %error of Area(mm*mm)
   end
```

```
Height=abs (y(end,1))*1000000, Width=2*t(end)*1000000,   % width unit changing m ---> um
area=2*y(end,2)*1e6,                    % (mm^2)
del_Area=100*del_Area*1e-6/A0       % error (%) of Area(mm*mm)
Porosity=(1-Q*1e6/(L_x*Height*V_n))
t=t*1000000;                            % width unit changing m ---> um
y=y*1000000;                            % height unit changing m ---> um
plot(t,y(:,1),'-');
grid;
text (1.4,-0.12,'Considering the Gravity Influence');
title ('Shape of Fluid Formed on Board');
xlabel ('Width (um)');
ylabel ('Height (um)');

% The END
```

[5]. Simulink model used in Program [4].

Shape Model (shape_model.mdl)

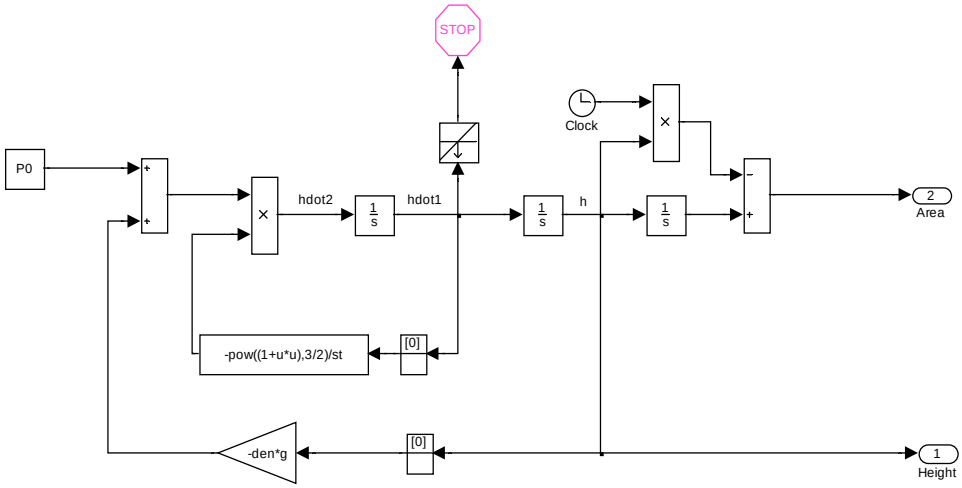

Notes:
1) The width is equal to the value of the time indicated by the Clock;
2) When the following situation occures, the simulation will stop:
hdot1 < -tan(sita*pi/180)